Nanomaterials characterization

Maria Kaliva, Maria Vamvakaki

Department of Materials Science and Technology, University of Crete, Heraklion, Greece; Institute
of Electronic Structure and Laser, Foundation for Research and Technology-Hellas,
Heraklion, Greece

17.1 Introduction

Nanomaterials, that have at least one dimension in the subnanometer to 10 nm range, present unique behavior when compared to their bulk counterparts, such as an exponential increase of their reactivity [1]. The distinct physicochemical features, that is, size, shape, composition, and surface properties of nanomaterials affect strongly their activity and performance. Physicochemical characterization of the nanomaterials can provide the basis for a better understanding of their complex structure-properties applications relationships [1, 2].

The precise determination of the properties of the nanomaterials is a very important area in nanotechnology and demands reliable and advanced techniques that are sensitive down to nanoscale dimensions [3]. In the last decades, nanomaterial characterization tools have been developed almost in parallel with the evolution of nanoscience and nanomaterials synthesis. The objective of this chapter is to present the main techniques available, which can be employed for the characterization of the nanomaterials' size, shape, chemical composition, surface charge, and optical, magnetic, and mechanical properties.

17.2 Size, shape, length, and internal structure characterization

The size and shape of nanomaterials are crucial characteristics that determine their physicochemical properties, which include their catalytic activity and bioactivity, their optical, magnetic, and mechanical properties, and so on. Dynamic light scattering (DLS), electron and force microscopies are among the most common techniques utilized to investigate the size, size distribution, shape, and aggregation state of nanomaterials.

17.2.1 Dynamic light scattering

DLS (also referred to as photon correlation spectroscopy and quasielastic scattering), one of the most popular light scattering modalities, is a fast, facile, and noninvasive technique, which uses a monochromatic wavelength light beam such as a laser, to measure the nanoparticles' size *in solution* or *suspension* [1, 4, 5].

When a particle is irradiated by a light source in the visible light range, part of the light is transmitted through the sample whereas another part can be absorbed by the sample [6]. When the particle size is small enough, relative to the wavelength (λ) of the incident irradiation ($<\lambda/20$), the irradiation will be scattered in all directions without a change in its energy or the wavelength of the incident light. This phenomenon is known as Rayleigh scattering, or elastic scattering of light, and is related only to the translational and rotational degrees of freedom of the particle [6]. The intensity of the light scattered by an individual particle is then given by the following equation:

$$I = I_o \frac{1 + \cos^2\theta}{2r^2} \left(\frac{2\pi}{\lambda}\right)^4 \left(\frac{n^2 - 1}{n^2 + 2}\right) \left(\frac{d}{2}\right)^6 \tag{17.1}$$

Where I_o and λ are the intensity and the wavelength of the incident light, respectively, r is the distance of the scattering center, θ is the angle at which the light is scattered, n is the refractive index, and d is the particle diameter.

The basic concept of the DLS technique is based on monitoring fluctuations of the Rayleigh scattering generated by the Brownian motion of the nanoparticles with size much smaller than the wavelength of the incident light, at a fixed scattering angle [7]. When a monochromatic light beam, such as a laser, shines in a solution containing randomly moving nanoparticles, the light is scattered with a different frequency which is related to the size of the particles. The particle size can be obtained from the analysis of the intensity fluctuation traces made up of constructive and destructive interferences of the scattered light using the motion-dependent autocorrelation function of Stokes-Einstein or the photon autocorrelation function. The main assumption of DLS is that the nanoparticles suspended in a fluid are moving in Brownian motion, which is also known as the "random walk" of the nanoparticles. This movement is a result of the random collisions of the particles with the solvent molecules that cause the particles to diffuse through the medium [7]. An important characteristic of Brownian motion regarding the DLS technique is that large particles move slower than smaller particles, meaning that the translational diffusion coefficient (D) of the particles is inversely related to their size, as given by the Stokes-Einstein equation (Eq. 17.2). The smaller particles are "kicked" further by the solvents molecules and move rapidly. Another important assumption is that the nanoparticles are spherical in shape, noninteracting, and small in size [7]. The size of the particle is calculated from the translational diffusion coefficient using the Stokes-Einstein equation:

$$R_h = \frac{kT}{6\pi nD} \tag{17.2}$$

where R_h is the hydrodynamic radius of the particles, k is the Boltzmann constant, T is the absolute temperature in Kelvin, n is the viscosity of the dispersing medium, and D is the translational diffusion coefficient. The particle diameter obtained by this technique is that

of a hard-sphere which has the same translational diffusion coefficient as the particle and is valid for spherical particles that do not interact among themselves.

Due to Brownian motion, the distance between the nanoparticles differs with time, resulting in constructive and destructive interferences in the intensity of the scattered light. Thus, the fluctuations of the scattered light intensity as a function of time provide information about the velocity of the scattering particles, that is, the translational diffusion coefficient. Larger particles will result in smaller fluctuation rates in the scattered light, whereas smaller, faster particles will cause higher fluctuation rates. The intensity fluctuations of the scattered light as a function of time can be then converted to values of the diffusion coefficient and the particle radius [6, 8]. The correlator used in the DLS experimental setup correlates the variation of the scattered intensity as a function of time to generate an autocorrelation function, $G(t)$, given by the following equation:

$$G(t) = < I(t_0)I(t_0 + t)$$ (17.3)

where $I(t_0)$ and $I(t_0 + t)$ are the numbers of the photons that reach the detector at the time (t_0) and after a time interval (t). For a large number of monodisperse particles in Brownian motion the correlation function is an exponential decay function with a characteristic relaxation time τ:

$$G(t) = A + Be^{-\frac{2t}{\tau}}$$ (17.4)

where the factor 2 indicates the homodyne method, A and B are parameters obtained by fitting the exponential points of the autocorrelation function [6]. In a typical DLS experiment, shown in Fig. 17.1, first a laser beam passes through a collimator lens and then impacts the solution containing the nanoparticles moving with Brownian motion and the light is scattered with a different frequency which is related to the nanoparticles' size. The scattered light is detected by a detector (photomultiplier which converts changes in the light intensity to voltage) at different angles [4, 7].

Another important characteristic of the nanoparticles that can be obtained from a DLS experiment is the polydispersity (PDI) of the sample. PDI can be determined from the widths of the particle size ranges and can be calculated using Eq. (17.5) when the particle size distribution can be fitted to a Gaussian distribution.

$$PDI = \frac{\sigma^2}{R_h^2}$$ (17.5)

Where σ is the standard deviation.

The value of the translational diffusion coefficient of a particle in a medium is dependent on how the particle moves in the medium. Therefore, the diameter obtained by DLS depends not only on the particle size but also on any surface structure, as well as the solvent, the concentration, and the type of electrolytes in the medium. Any change on the surface of the particle, which affects its diffusion speed will correspondingly change the apparent size of the particle [10]. For example, an absorbed polymer layer on the nanoparticle surface will reduce the diffusion speed of the nanoparticle, and therefore will increase the size obtained by DLS. In Fig. 17.2 the increase of the average hydrodynamic diameter of gold nanoparticles, modified with polystyrene brushes of different molecular weights, is presented. As the
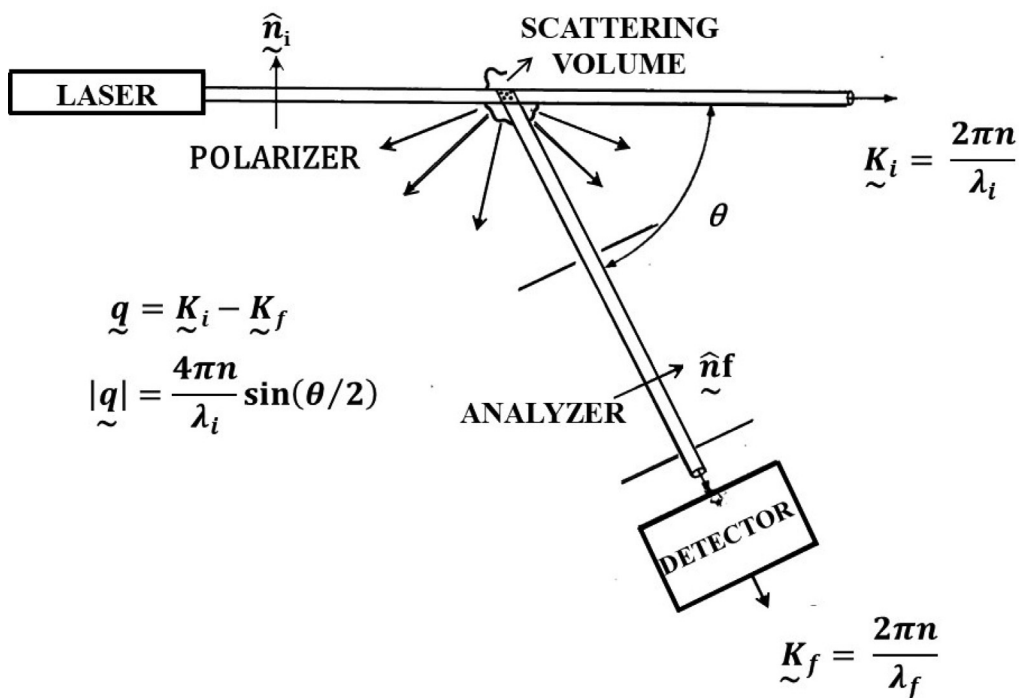
$\hat{n}_i$

SCATTERING VOLUME

LASER

POLARIZER

$K_i = \dfrac{2\pi n}{\lambda_i}$

θ

$\underset{\sim}{q} = \underset{\sim}{K}_i - \underset{\sim}{K}_f$

$|\underset{\sim}{q}| = \dfrac{4\pi n}{\lambda_i}\sin(\theta/2)$

$\hat{n}f$

ANALYZER

DETECTOR

$K_f = \dfrac{2\pi n}{\lambda_f}$

FIG. 17.1　Schematic representation of the experimental setup used in DLS measurements [9]. *Reproduced with permission from J.B. Berne, R. Pecora. Dynamic Light Scattering: With Applications to Chemistry, Biology, and Physics, 2000. Copyright (2000), John wiley & Sons Inc.*
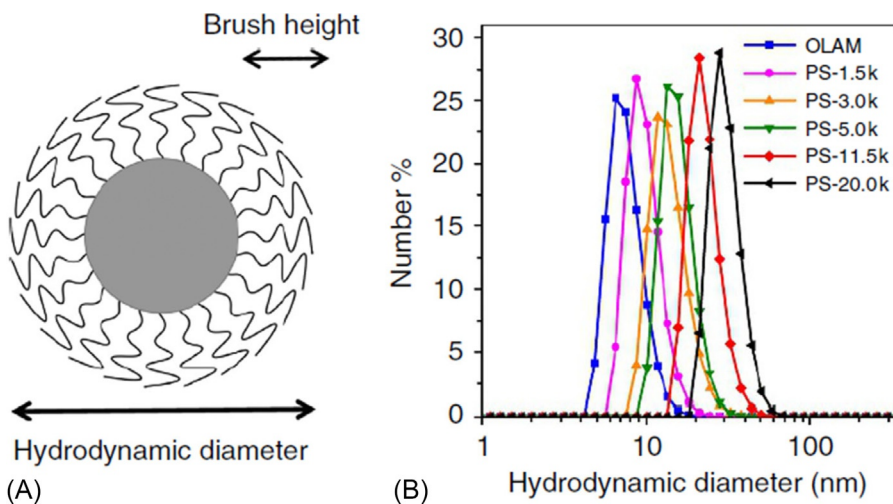

FIG. 17.2　Gold nanoparticles modified with polystyrene brushes (A) and average hydrodynamic diameter of gold nanoparticles modified with polystyrene brushes of different molecular weights (B) [11]. *Reproduced with permission from X. Ye, C. Zhu, P. Ercius, S.N. Raja, B. He, M.R. Jones, et al., Structural diversity in binary superlattices self-assembled from polymer-grafted nanocrystals, Nat. Commun. 6 (2015) 10052. Copyright (2015), Springer Nature.*

II. Nanotechnology

molecular weight of the polystyrene chain increases, the average hydrodynamic diameter of the polymer-modified gold nanoparticles also increases.

The stability of the particles can be also studied as nanoparticle aggregates will give a larger particle size in DLS. The technique has been used to determine the minimum amount of stabilizing agent required to prevent nanoparticle aggregation [12]. Moreover, the encapsulation efficiency of drugs within polymer micelles and liposomes, acting as controlled drug delivery systems, has been determined by DLS measurements [13, 14].

On the other hand, DLS has also several limitations. The technique has limited use in the analysis of samples with a heterogeneous size distribution, and in a mixed sample, populations vary in size by a factor or less than three [1, 15]. Furthermore, DLS is not appropriate to determine the precise size of nanoparticles of nonspherical geometries, since the spherical nature of the particles is assumed in the analysis discussed earlier, and more complicated measurements and analyses are used in this case, which is beyond the scope of this chapter. Finally, the size obtained by DLS is depended on the concentration of the particles (an accurate size is determined in very dilute samples) and the type and concentration of ions present in the solution [6, 16].

17.2.2 Microscopy

Advanced microscopy techniques such as scanning and transmission electron microscopy and atom force microscopy are employed to examine and visualize structural details of nanomaterials that cannot be observed by the naked eye. They allow the visualization of nanoparticles or structures present within the nanoparticles or on its surface, depending on the technique used and the characteristics of the sample [17]. While optical microscopes use visible light sources and lenses to produce magnified images at the micrometer scale, electron microscopes (EM) utilize beams of accelerated electrons and electrostatic or electromagnetic lenses to generate images of much higher resolution, based on the much shorter wavelengths of electrons compared to the light photons [1, 3, 18].

17.2.2.1 *Scanning electron microscopy*

Scanning electron microscopy (SEM) is a surface-imaging technique, which generates high-resolution and high magnification images of a sample by scanning its surface with a focused electron beam. SEM can resolve up to 1 nm and can magnify up to $400,000 \times$ [3]. The incident electron beam, with a negative charge, interacts with the material that has a specific arrangement and electron clouds and produces various signals reflecting the topographic detail and the atomic composition of the scanned specimen surface [7]. The incident electron beam causes the emission of X-rays from the atoms on the surface of the sample, of elastically backscattered (or primary) electrons, secondary inelastic electrons, and Auger electrons. Secondary electrons are the most valuable for obtaining the sample morphology/topography. From the secondary electrons, high-resolution images can be produced revealing details of around 1–5 nm, while characteristic X-rays are used by a technique known as energy dispersive X-Ray analysis (EDX) to identify the elemental composition and Auger electrons are used in surface analytical techniques [2, 7, 19].
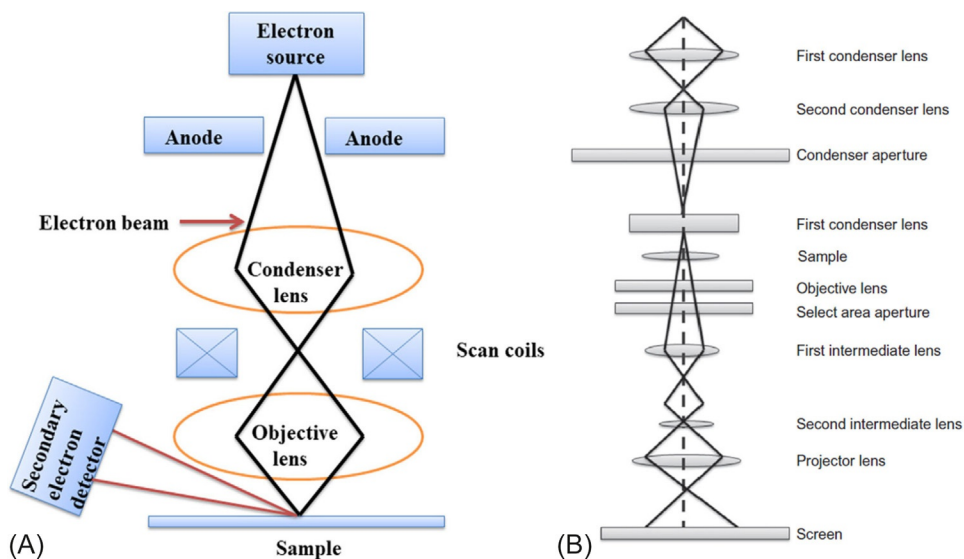
FIG. 17.3   (A) Scanning and (B) transmission electron microscopies [2]. *Reproduced with permission from D. Titus, E. James Jebaseelan Samuel, S.M. Roopan, Nanoparticle characterization techniques, in: A.K. Shukla, S. Iravani (Eds.), Green Synthesis, Characterization and Applications of Nanoparticles, Elsevier, 2019, pp. 303–319 (Chapter 12). Copyright (2019), Elsevier.*

A typical schematic diagram of an SEM is presented in Fig. 17.3A. An electron gun located at the top of the instrument emits electrons. The two main electron gun types are field emission guns (FEG), which produce a strong electric field that rips electrons from the atoms, and thermionic guns, in which the filament is heated until the electrons stream away (Tungsten (W) filament and solid-state crystals (CeB6 or LaB6) are typically used). These electrons are then accelerated to a voltage between 1 and 40 kV and condensed into a narrow beam, which is used for imaging and analysis. At optimum operation, an accelerating voltage of 20–25 kV is used. If the accelerating voltage is low (2.5–10 kV), the chromatic aberration of the incident beam is high, which results in extremely poor resolution, while, if the accelerating voltage is high in the range of 30–50 kV, the size of the spot increases and the beam can penetrate the sample, enlarging the zone of internal scattering that generates backscattered electrons. The sample is located near the lower end of the column [7].

The electrons first pass through two or more electromagnetic lenses that focus the electron beam into a small spot, which determines the instrument resolution (the smaller the spot, the higher is the resolution). Next, the fine beam of electrons is scanned across the specimen by scan coils, while a detector counts the number of low energy secondary electrons, or other radiations, emitted from the surface of the specimen. The image is displayed on a cathode-ray tube by the raster method. The displayed image is a distribution map of signal intensity emitted from the scanned area of the specimen. The instrument is operated under a high vacuum to produce the high energy electron beam because electrons can travel only a small distance through air [7].

In SEM, the surface of the sample must be electrically conductive and grounded to prevent the accumulation of electrostatic charge at the surface, which leads to electrostatically distorted images and artifacts. For this, the surface of nonconductive samples is coated with an ultrathin layer of an electrically conducting material, such as Au, Au/Pd alloys, and Pt [4]. Furthermore, in conventional SEM it is also important to remove the water from the sample since water molecules will evaporate under vacuum and destroy the clarity of the image [2]. The recently developed environmental scanning electron microscope (ESEM) is designed to operate under a lower vacuum and lower voltage. ESEM is useful to visualize specimens under their "natural" form, with minimum sample preparation. This includes the ability to examine moist samples, such as biological specimens.[1, 18].

SEM is often combined with the EDX technique, which is used to analyze the elements present near the surface in the micrometer scale and to determine the elemental composition at different positions. SEM-EDX is a very useful technique because at relatively short time information regarding the size, shape, surface texture and elemental analysis can be obtained. By EDX analysis nanoparticles such as silver, gold, and palladium can be easily identified on the surface of a sample. However, elements of a low atomic number are harder to detect by EDX [4].

In a field emission SEM (FESEM), a FEG produces high-primary electron brightness and small spot size even at low accelerating potentials, causing less charging of the surface. Compared to conventional SEM, FESEM produces clearer and less electrostatically distorted images, with a spatial resolution down to 20 nm, which is three to six times better than conventional SEM [4, 18].

SEM can provide information about the shape, the size, and the size distribution of nanomaterials. The size of the particles obtained by SEM usually corresponds to the mean Feret diameter of the projected equivalent surface diameter (dS) of a disc of area S. For spherical particles, dS is given by the following equation [20]:

$$dS(\text{nm}) = 2\sqrt{\frac{S}{\pi}}\ (\text{nm}) \tag{17.6}$$

Fig. 17.4 shows characteristic FESEM images of ZnO disc-twin-spheres with topological surfaces (A, B) [21] and jelly-like silica nanoparticles (C, D), in which details of the nanoparticle structure are evident [22].

However, there is some limitation in the SEM measurements. During sample preparation, the process of drying and contrasting may cause the shrinkage of the nanomaterials which changes their features in terms of size and shape. Besides, due to the small number of particles present in the scanning region, biased statistics of the size-distribution of heterogeneous samples are inevitable [1].

17.2.2.2 Transmission electron microscopy

Transmission electron microscopy (TEM) is another electron microscopy technique frequently used for the characterization of the nanomaterials. TEM can provide direct high-resolution images and detailed qualitative/quantitative chemical information for the nanomaterials at a spatial resolution down to atomic dimensions (<1 nm) [1].
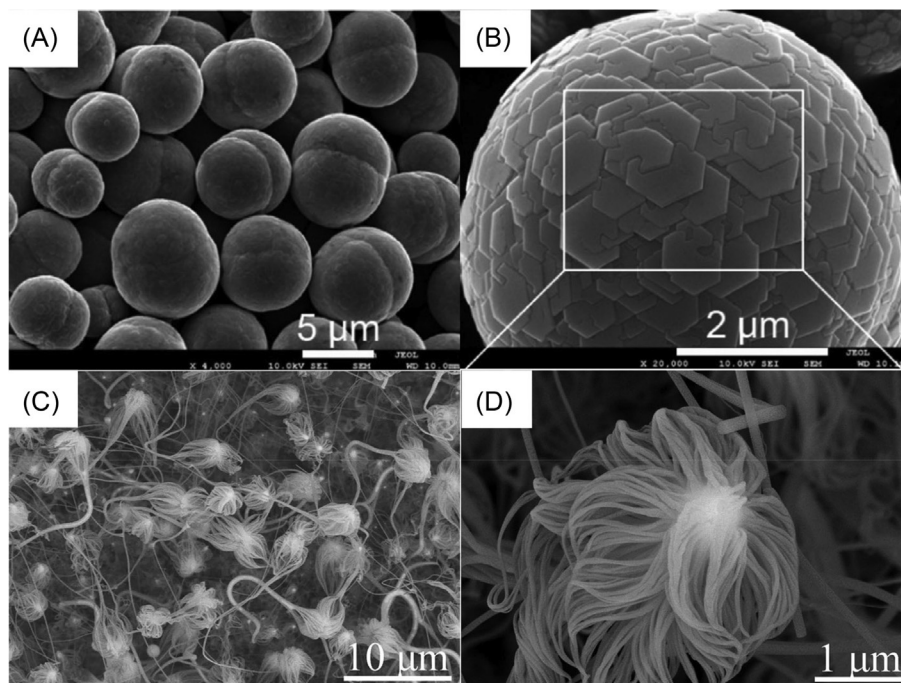
FIG. 17.4   Low magnification (A, C) and high magnification (B, D) FESEM images of ZnO disc-twin-spheres [21] and jellyfish-like silica nanoparticles [22]. *Reproduced with permission from F. Li, F. Gong, Y. Xiao, A. Zhang, J. Zhao, S. Fang, et al., ZnO Twin-spheres exposed in ±(001) facets: stepwise self-assembly growth and anisotropic blue emission, ACS Nano 7 (2013) 10482–10491. Copyright (2013), American Chemical Society) and H. Liu, Z. Huang, J. Huang, S. Xu, M. Fang, Y.-g. Liu, et al., Morphology controlling method for amorphous silica nanoparticles and jellyfish-like nanowires and their luminescence properties, Sci. Rep. 6 (2016) 22459. Copyright (2016), Spinger Nature.*

While the constituents of a TEM are similar to those of a conventional SEM, with the arrangement of the electron gun and electromagnetic lenses, condenser, etc., the basic difference is in the sample specimen and its position and on the way that the data are collected from the sample (Fig. 17.3B). In TEM, an incident high-energy electron beam is transmitted through an ultra-thin specimen. As the electron beam enters the thin specimen, electron-electron interactions between the beam and the sample transform the incident electrons into unscattered, elastically scattered, or inelastically scattered electrons. The scattered or unscattered electrons are focused on a series of electromagnetic lenses and then projected on a screen to generate electron diffraction, amplitude-contrast image, a phase-contrast image, or a shadow image of variable darkness based on the density of unscattered electrons [7]. TEM magnification is mostly estimated by the ratio of the distance between the objective lens and the specimen and the distance between the objective lens and its image plane [1].

Ultrathin sample sections, generally less than 1 μm, are required in TEM to allow the electrons to penetrate through the samples. Materials that have dimensions small enough to be electrons transparent, such as powders, nanoparticles, and nanotubes, can be easily prepared by the deposition of a dilute sample containing the particles onto supported grids. In some cases, samples are cut into thin films with a diamond knife under cryogenic conditions, known as cryo-microtome [2, 4].

TEM is operated under a high vacuum to transmit the electron beam. A high vacuum is required to avoid the deflection or attenuation of the electron beam by gas molecules in the air. The electron beam is deflected by the variable electron densities around the atoms within the specimen. High atomic number elements having greater electron densities show the greatest contrast. The contrast of substances containing low atomic number elements such as biological and polymeric nanostructured samples and blends can be enhanced by the selective absorption of high atomic number elements into one region, phase, or component of interest. A typical staining reagent is osmium tetroxide which is selectively absorbed by unsaturated bonds [3].

High-resolution TEM (HR-TEM) is an imaging mode of TEM that allows the direct imaging of the crystallographic structure of a sample at the atomic level. HR-TEM is a powerful tool to study the properties of materials on the atomic scale and it enables the visualization of crystal structures, crystal defects as well as individual atoms. HR-TEM can be employed to study crystal nanoparticles and their arrangement in the specimen, nanocrystalline features in amorphous films, nanofibers, and their alignment and porous materials [2, 4, 18]. Typical TEM and HR-TEM images of metallic, polymeric, hybrid, and porous nanoparticles are presented in Fig. 17.5. The size, shape, and crystallographic structure of the nanomaterials are observed.

In addition to the high spatial resolution of TEM, a wide range of analytical techniques can be coupled with TEM for qualitative and quantitative chemical analyses of the tested sample. The main analytical techniques are the energy-dispersive X-ray spectroscopy (EDX), electron
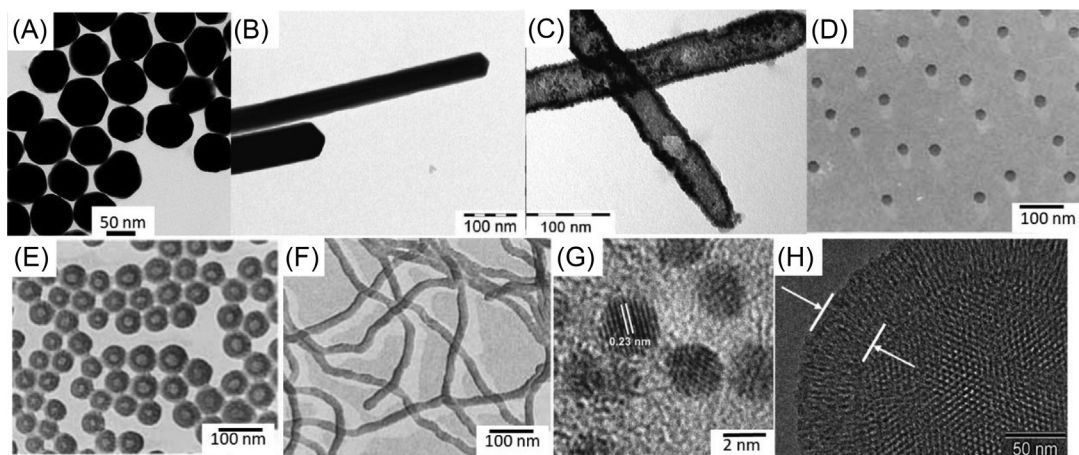

FIG. 17.5 TEM images of AuNPs (A) [23], Cu nanotubes (B), CuPt nanotubes (C) [24] polymeric micelles (D), vesicles (E) and worm-like micelles (F) [25] and HR-TEM images of thiol capped Au nanoparticles (G), and a mesoporous nanomaterial (H) [26]. *Reproduced with permission from M.A.C. Potenza, Ž. Krpetić, T. Sanvito, Q. Cai, M. Monopoli, J.M. de Araújo, et al., Detecting the shape of anisotropic gold nanoparticles in dispersion with single particle extinction and scattering, Nanoscale 9 (2017) 2778–2784. Copyright (2017), Royal Society of Chemistry, M. Mohl, D. Dobo, A. Kukovecz, Z. Konya, K. Kordas, J. Wei, et al., Formation of CuPd and CuPt bimetallic nanotubes by galvanic replacement reaction, J. Phys. Chem. C 115 (2011) 9403–9409. Copyright (2011), American Chemical Society, L. Zhang, A. Eisenberg, Formation of crew-cut aggregates of various morphologies from amphiphilic block copolymers in solution, Polym. Adv. Technol. 9 (1998) 677–699. Copyright (1998), John Wiley & Sons Ltd. A.E. Garcia-Bennett, O. Terasaki, S. Che, T. Tatsumi, Structural investigations of AMS-n mesoporous materials by transmission electron microscopy, Chem. Mater. 16 (2004) 813–821. Copyright (2004), American Chemical Society.*

energy loss spectroscopy (EELS), and energy-filtered transmission electron microscopy (EFTEM). Chemical analysis by EELS and EDX can quantitatively investigate the electronic structure and chemical composition of nanomaterials, respectively, whereas, EFTEM can be used to produce elemental distribution maps of the sample within short acquisition times and at high resolution, rendering it an efficient tool for the detailed characterization of nanostructures [4, 27].

Although TEM is a powerful technique to investigate the shape, size, and heterogeneity of nanomaterials, as well as the degree of aggregation and dispersion, it presents certain drawbacks. The first important drawback is the requirement of high vacuum and ultrathin sample sections for TEM measurements. The preparation of thin specimens increases the possibility of altering the structure of the sample. Besides, the high-voltage electron beam can damage or even destroy the specimen. Artifacts can also be produced while probing 3D specimens by the 2D TEM technique in transmission view, due to the lack of depth sensitivity in a single TEM image. Finally, similar to SEM, TEM provides poor statistical analysis as a result of the examination of a small area of the specimen over a certain period [1, 3].

17.2.2.3 Atomic force microscopy

Atomic force microscopy (AFM) or scanning probe microscope (SPM) is a mechanical imaging technique used widely for the analysis at the nanoscale and gives information about the three-dimensional (3D) topography of a specimen. Similar to TEM and SEM, AFM can be used to investigate the shape, size, structure, and degree of dispersion of nanomaterials [2]. However, AFM provides several advantages over conventional microscopy techniques. It performs measurements in three dimensions x, y, and z (normal to the sample surface), thus enabling the presentation of 3D images of the sample. The resolution can be similar to TEM, ranging from 0.1 to 1.0 nm in the x-y plane and is 0.01 nm (atomic resolution) in the z-direction. It does not require conductive surfaces or any special sample preparation processes. AFM operates either at ambient conditions or in a liquid environment [3, 18, 28].

The topography image is obtained by the scan of the probe on the surface of a specimen using a sharp tip, located at the free end of a cantilever. The process is based on the interatomic forces between the sample and the tip. AFM can measure a range of tip-surface interactions, depending on the distance between the tip and the sample. At short distances, the tip predominantly experiences interatomic forces: very short range ($\sim$0.1 nm) Born repulsive forces and longer range (up to 10 nm) van der Waals forces. At larger distances from the surface (100–500 nm above the surface), long-range electric, magnetic, and capillary forces can be probed [4, 18].

The AFM setup consists of a cantilever with a sharp mechanical tip (probe) at its end, which is used to scan the surface of a specimen. The tips are commonly fabricated from silicon or silicon nitride with a radius of curvature in the order of nanometers. The tip is positioned close enough to the surface such that it can interact with the force fields associated with the surface, which leads to a deflection of the cantilever according to Hook's law:

$$F = -k\Delta z \qquad (17.7)$$

where F is the force, k is the spring constant of the cantilever, and z is the bending distance of the cantilever [28].

The AFM head comprises an optical detection system in which a diode laser is focused onto the back of the reflective cantilever. As the tip scans the surface of the sample, moving with the contour of the surface, the laser beam is deflected off the cantilever into an array of photodiodes. In most cases, a feedback mechanism is employed to adjust the tip-sample distance and to maintain a constant force between the tip and the sample. The sample is mounted on a piezoelectric scanner, which moves it in the z-direction, therefore maintaining a constant force or a constant height above the sample (Fig. 17.6).

AFM can be operated in several modes, depending on the application. In general, all possible imaging modes are divided into contact modes and noncontact modes, in which the cantilever is vibrated. Contact mode is when the probe is drawn across the surface, progressively scanning in rows. However, contact with the surface may cause damage to the surface. Tapping modes involve intermittent contact as the probe is oscillated vertically to and from the surface during scanning. Other modes include noncontact modes when interactions or current occur between the probe tip and the surface [4, 28]. Typical AFM images of soft and hard nanomaterials are depicted in Fig. 17.7.

In addition to investigating the shape and size of nanomaterials, AFM is capable of characterizing surface features, surface roughness, and the dynamics of nanomaterials in real-time, for example, biological systems [1]. AFM can image biomaterials without causing significant damage to their surface and can measure other position-related properties such as surface friction, hardness, electrical, and thermal conductivity [3, 4]. The main advantage of AFM is its capability to image a variety of nanomaterials at the subnanometer scale under environmental conditions or even immersed in fluids [4]. However, the main disadvantage of AFM is that the size of the cantilever tip is larger than the dimensions of the nanomaterials examined, resulting in an overestimation of the lateral dimensions of the sample. Moreover, AFM is not capable of detecting or locating specific molecules. However, this drawback has been eliminated by recent progress in single-molecule force spectroscopy which uses an AFM cantilever tip modified with a small molecule, a cell adhesion molecule, or a chemical group, which can probe or detect single functional molecules on a surface [1].
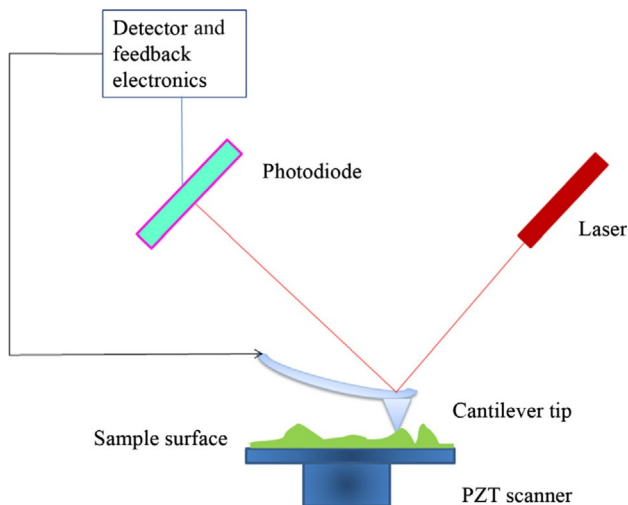

FIG. 17.6 Schematic representation of an atomic force microscope [2]. *Reproduced with permission from D. Titus, E. James Jebaseelan Samuel, S.M. Roopan, Nanoparticle characterization techniques, in: A.K. Shukla, S. Iravani (Eds.), Green Synthesis, Characterization and Applications of Nanoparticles, Elsevier, 2019, pp. 303–319 (Chapter 12). Copyright (2019), Elsevier.*
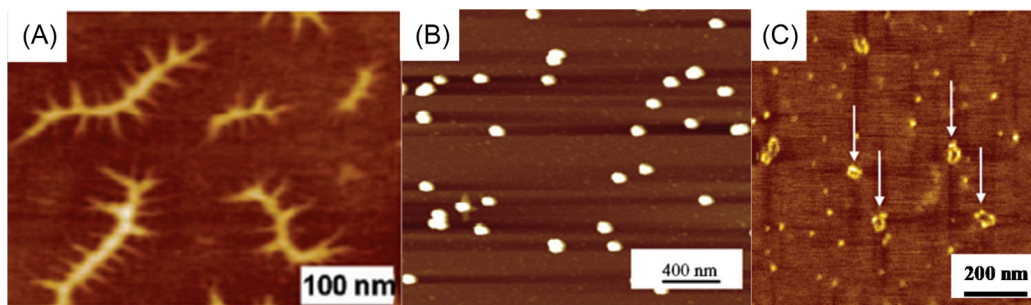
FIG. 17.7   AFM images of molecular polymer brushes (A) [29], Au nanoparticles (B) [30], and cyclic poly(sodium styrenesulfonate) chains (C) [31]. *Reproduced with permission from S.Y. Yu-Su, S.S. Sheiko, H.-i. Lee, W. Jakubowski, A. Nese, K. Matyjaszewski, et al., Crystallization of molecular brushes with block copolymer side chains, Macromolecules 42 (2009) 9008–9017. Copyright (2009), American Chemical Society, M. Baalousha, J.R. Lead, Rationalizing nanomaterial sizes measured by atomic force microscopy, flow field-flow fractionation, and dynamic light scattering: sample preparation, polydispersity, and particle structure, Environ. Sci. Technol. 46 (2012) 6134–6142. Copyright (2012), American Chemical Society, D. Kawaguchi, T. Nishu, A. Takano, Y. Matsushita, Direct observation of an isolated cyclic sodium poly(styrenesulfonate) molecule by atomic force microscopy, Polym. J. 39 (2007) 271–275. Copyright (2007), Springer Nature.*

17.3 Surface charge characterization of nanoparticles (zeta potential measurements)

The surface charge of nanoparticles is commonly considered among the most important parameters that determine the properties of the nanomaterials. The surface charge affects the dispersion stability and aggregation state of the nanomaterials. Particles with high positive or negative surface charge tend to repel each other and form a stable colloidal dispersion while nanoparticles with low surface charge often agglomerate and precipitate. Zeta potential measurements determine the surface charge of nanoparticles in a colloidal solution [32, 33].

Nanoparticles with a net charge on their surface attract a thin layer of counterions that are strongly bound on their surface (Stern layer). This layer is surrounded by an outer diffuse layer that consists of loosely associated ions. Thus, these two layers form the so-called electrical double layer (Fig. 17.8). As the particle moves due to Brownian diffusion or to external forces, a gradient is created between the ions in the diffuse layer that move with the nanoparticle and those that remain within the dispersion medium. The electrical potential at this boundary is called zeta potential and is related to the surface charge of the nanoparticle [1, 35].

The zeta potential can be determined by measuring the movement of a nanoparticle in an electrical field that is electrophoretic mobility. The zeta potential (ζ) is calculated from the Henry equation:

$$\mu_\varepsilon = \frac{2\varepsilon\zeta}{3n}f(ka) \tag{17.8}$$

where μ_ε is the electrophoretic mobility, ε is the dielectric constant, n is the absolute zero-shear viscosity of the medium, $f(ka)$ is the Henry function, and ka is a measure of the ratio of the particle radius to the Debye length.
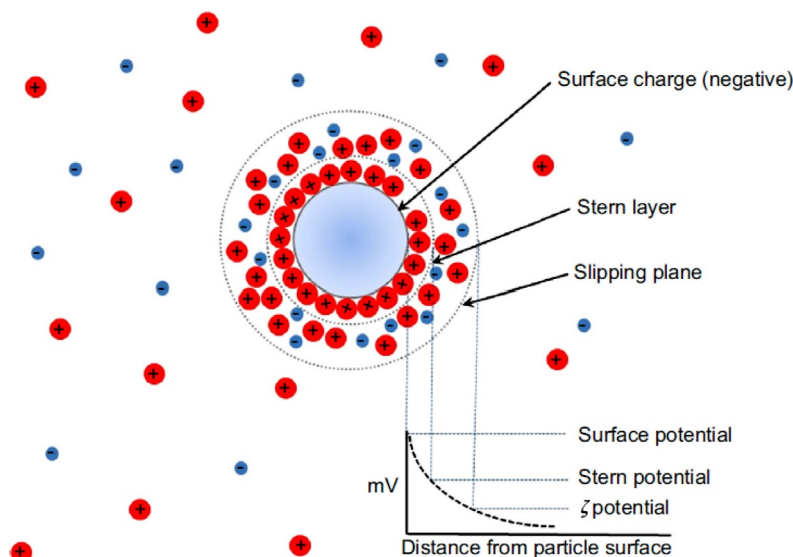
FIG. 17.8 Schematic representation of the electrical double layer of a particle suspended in a liquid [34]. *Reproduced with permission from K. Pate, P. Safier, Chemical metrology methods for CMP quality, in: S. Babu (Ed.), Advances in Chemical Mechanical Planarization (CMP), Woodhead Publishing, 2016, pp. 299–325 (Chapter 12). Copyright (2016), Woodhead Publishing.*

Zeta potential is an important tool for estimating the surface charge of the nanoparticles and its magnitude is used to predict their colloidal stability in solution [2, 35]. Zeta potential can take values in the range of +100 to −100 mV. In general, nanoparticles with zeta potential values greater than +30 mV or less than −30 mV are considered strongly cationic and anionic, respectively and show high degrees of colloidal stability, whereas, nanoparticles with zeta potential below +25 mV or greater than −25 mV tend to agglomerate due to interparticle interactions, including van der Waals, hydrophobic and hydrogen bonding interactions. Last, nanoparticles with a zeta potential value between 10 and +10 mV are considered approximately neutral.

Zeta potential measurements are typically used to assess the successful coating of nanomaterials via the polyelectrolyte layer-by-layer self-assembly process (Fig. 17.9A), in which the surface charge of the particles is switched between positive and negative values upon successive adsorption of the polycationic and polyanionic polymers [36]. The technique is also employed to determine the pH-responsive behavior of weak polyelectrolyte particles and therefore, assess their stability as a function of the pH of the medium (Fig. 17.9B) [37].

Among the existing methods to calculate the zeta potential, electrophoretic light scattering (ELS) is the most commonly used technique, due to its high sensitivity, accuracy, and versatility. Conventional ELS, cannot be applied for turbid samples since the incident light cannot penetrate them. Furthermore, zeta potential is a feature that is not only affected by the nanoparticles, but also by the environment in which the particles are suspended, including the solution pH and ionic strength. Therefore, an accurate and reproducible zeta potential

FIG. 17.9 Zeta-potential analysis at each step of polyelectrolyte (poly(allylamine hydrochloride) and poly(styrenesulfonate)/tetrapyrrolic dye meso-tetrakis(4-sulfonatophenyl)porphine) adsorption (A) [36] and zeta potential values for cationic, pH-responsive polymeric micelles as a function of the solution pH (B) [37]. *Reproduced with permission from M.F. Bédard, S. Sadasivan, G.B. Sukhorukov, A. Skirtach, Assembling polyelectrolytes and porphyrins into hollow capsules with laser-responsive oxidative properties, J. Mater. Chem. 19 (2009) 2226–2233. Copyright (2009), Royal Society of Chemsitry, C. Yang, J. Xiao, W. Xiao, W. Lin, J. Chen, Q. Chen, et al., Fabrication of PDEAEMA-based pH-responsive mixed micelles for application in controlled doxorubicin release, RSC Adv. 7 (2017) 27564–27573. Copyright (2017), Royal Society of Chemsitry.*

measurement in a diluted suspension cannot reflect the correct value in a concentrated suspension [1]. In general, traditional ELS cannot be applied for dispersions with a concentration higher than 0.01%, whereas, for concentrated colloidal suspensions, the transparent electrode technology has been employed to obtain consistent and precise zeta potential values [38].

17.4 Optical properties

Nanoparticles and nanostructured materials often exhibit optical properties that are very sensitive to their size, shape, agglomeration state, and concentration. Ultraviolet-visible (UV-Vis) and fluorescence spectroscopies are among the most useful optical techniques for studying the optical properties of nanomaterials, allowing us to reveal important features of the nanomaterials, without notably modifying or permanently damaging them, since they are noncontact and noninvasive techniques [4, 39].

17.4.1 Ultraviolet-visible spectroscopy

UV-Vis spectroscopy, also known as electronic absorption spectroscopy, is based on the measurement of the light absorbed due to electronic transitions in a sample and is widely used in nanomaterial characterization. The wavelength (λ) of light required for electronic transitions is typically in the ultraviolet (200–390 nm) and visible (390–780 nm) region of the electromagnetic radiation spectrum [16].

In UV-Vis spectroscopy, the intensity of light (I) that passes through the sample is measured. When the light beam passes through a solution, a part of it may be absorbed, while the rest will be transmitted through the solution. The ratio of the intensity of the transmitted light (I) to the intensity of the incident light (I_o) entering the sample at a fixed wavelength is called transmittance (T) ($T = \frac{I}{I_o}$), while the negative logarithm of transmittance is called absorbance (A) ($A = -logT$). The energy of radiation that is absorbed is equal to the energy difference between the ground state and the higher energy state of the electron. In general, the electronic transition from the highest occupied molecular orbital to the lowest unoccupied molecular orbital is favored [4, 16, 40].

UV-Vis spectroscopy obeys the Beer-Lambert law, which says that when a monochromatic light beam passes through a solution of an absorbing sample, the absorbance (A) is directly proportional to the concentration (C) of the absorbing substance and the path length (l), and is given by the following equation:

$$A = \log\left(\frac{I_o}{I}\right) = \varepsilon l C \tag{17.9}$$

where ε is the molar absorption or extinction coefficient that is characteristic of a given compound under defined conditions (wavelength, solvent, and temperature) ($mol^{-1}/dm^{-3}cm$), l the path length in centimeters, and C is the concentration in $mol\,dm^{-3}$ [16]. The molar absorption coefficient (ε) is characteristic of a given molecule under a precisely defined set of conditions, wavelength, solvent, and temperature and is independent of the concentration and the path length [40].

A spectrophotometer is the instrument used for measuring the transmittance or absorbance of a sample as a function of the wavelength of the electromagnetic radiation and consists of a deuterium and tungsten lamp, for the ultraviolet and visible region wavelengths, respectively, a sample cell, a reference cell, a detector, and a monochromator (Fig. 17.10). In UV-Vis spectroscopy, the polychromatic light generated from the source is focused on the entrance slit of a monochromator, which selectively transmits a narrow band of light. This light then passes through the sample area to the detector. The absorbance of the sample is determined by measuring the intensity of the light reaching the detector after passing through the sample (sample cell) and comparing it to the intensity of light that reaches the detector without passing through the sample (reference cell) [2].

UV-Vis spectroscopy is a fast, simple, and sensitive technique that can give valuable information about nanomaterials. It can be used to investigate the size and oxidation state of carbon nanotubes or to determine the size and shape of metal nanoparticles. The bandwidth of the absorption spectrum, the intensity, and the wavelength peak of the surface plasmon resonance of metal nanoparticles depends on their composition, size, shape, and aggregation state (Fig. 17.11A) [2, 4, 16, 40, 42, 43]. For example, the absorption spectra of metal nanoparticles shift toward longer wavelengths as the nanoparticle size increases (Fig. 17.11B).

The electronic spectra of semiconducting nanoparticles are directly linked to the energy bandgap (ΔE) of the nanoparticles and are related to the size of the nanoparticles by the following equation [44]:

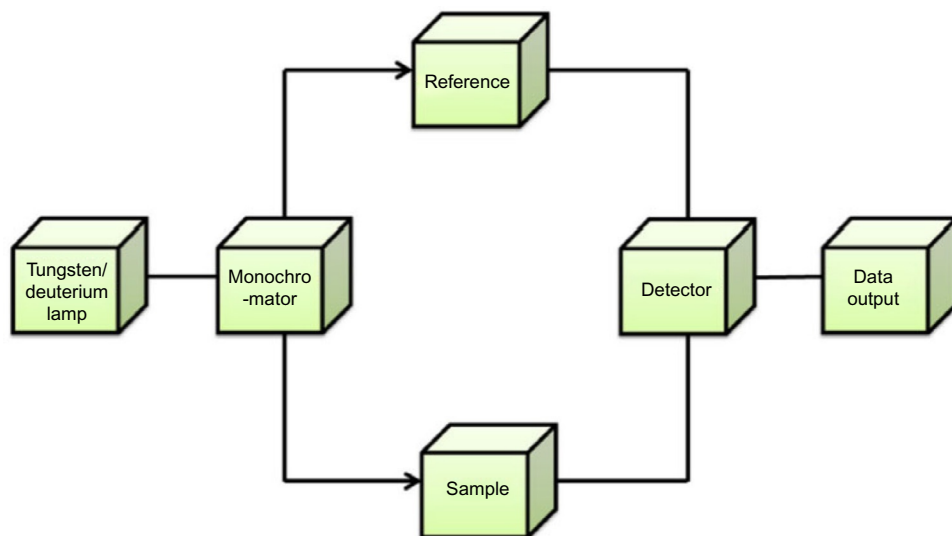$$\Delta E = \frac{n^2h^2}{8ma} \tag{17.10}$$

FIG. 17.10   Schematic representation of a UV-Vis spectrophotometer [2]. *Reproduced with permission from D. Titus, E. James Jebaseelan Samuel, S.M. Roopan, Nanoparticle characterization techniques, in: A.K. Shukla, S. Iravani (Eds.), Green Synthesis, Characterization and Applications of Nanoparticles, Elsevier, 2019, pp. 303–319 (Chapter 12). Copyright (2019), Elsevier.*
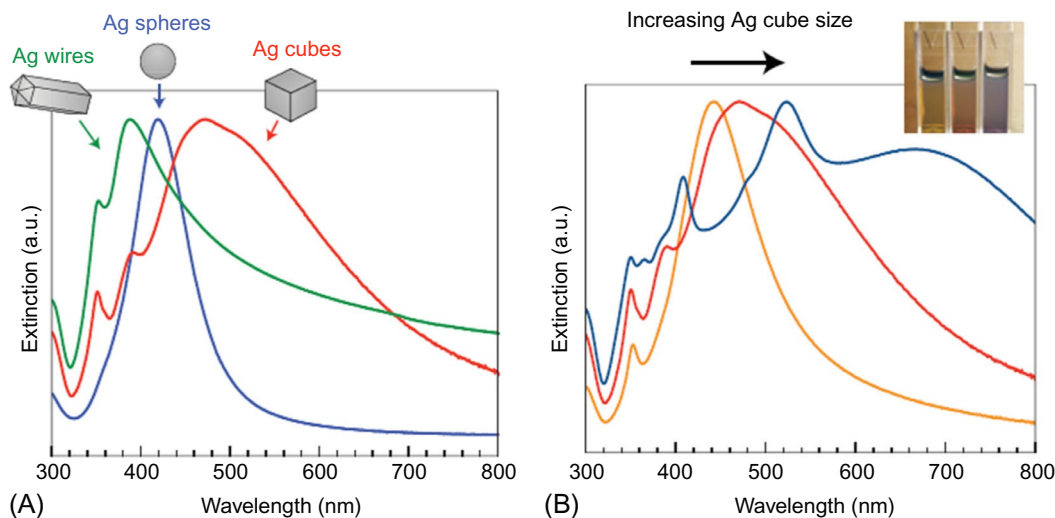

FIG. 17.11   Normalized extinction spectra for Ag nanoparticles of different shapes (A) and normalized extinction spectra for Ag nanocubes as a function of their size (B) [41]. *Reproduced with permission from S. Linic, P. Christopher, D.B. Ingram, Plasmonic-metal nanostructures for efficient conversion of solar to chemical energy, Nat. Mater. 10 (2011) 911. Copyright (2011), Springer Nature.*

where η is the principal quantum number, h is the Planck's constant, m is the effective mass of an electron, and α is the radius of the QDs. A decrease in the diameter of the semiconducting nanoparticles causes a blueshift of the band edge of absorption [4, 42, 43].

UV-Vis spectroscopy can be also used to monitor the stability of the nanoparticles in solution and to determine the extent of nanoparticle aggregation since the original extinction peak will be reduced in intensity and often the band will broaden, or a secondary band will appear at longer wavelengths as the particles agglomerate [16].

17.4.2 Fluorescence spectroscopy

Fluorescence spectroscopy also referred to as fluorometry or spectrofluorometry, is a complementary technique to the electronic absorption spectroscopy and analyzes the fluorescence from a sample [16]. Fluorescence is a photon emission process that occurs upon molecular relaxation from an electronically excited state to an electronic ground state. Molecules with the ability to fluoresce are known as fluorescence dyes, fluorophores, or fluorochromes. The main principles of fluorescence are presented by the Jablonski diagram (Fig. 17.12) [16]. When a fluorescence molecule or nanostructured material absorbs a photon, the molecule goes to an excited state by the transfer of an electron from the singlet ground state (S0) to an excited singlet state (Sn), where $n > 1$. This excitation process is very fast [4, 16]. After excitation, the molecule relaxes quickly to the lowest vibrational level of the excited electronic state, by dissipating part of its energy to the surrounding environment. This vibrational relaxation is a rapid process and occurs on a timescale of femtoseconds to a picosecond. Finally, emission occurs, typically after 10^{-8} s after the excitation, during which the electron returns to its more stable allowed ground state (S0), thereby emitting light at a wavelength which corresponds to the difference in energy between the two electronic states (Fig. 17.12).
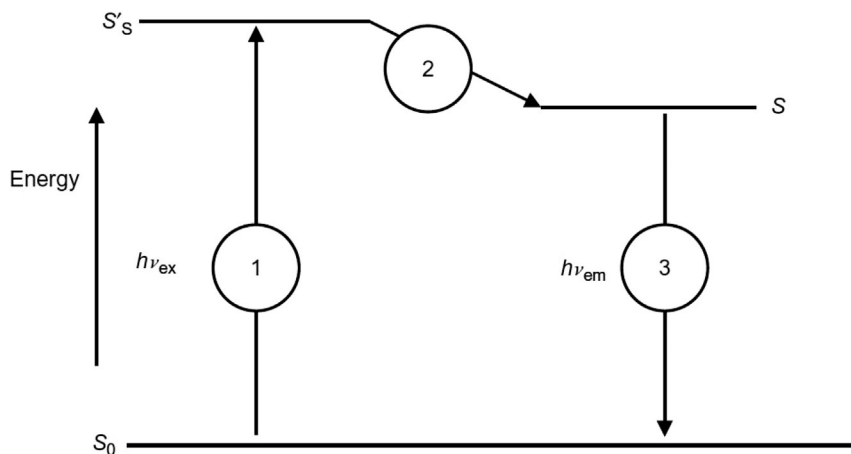

FIG. 17.12 Jablonski diagram showing the basic principle in fluorescence spectroscopy [45]. *Reproduced with permission from R. Karoui, Spectroscopic technique: fluorescence and ultraviolet-visible (UV-Vis) spectroscopies, in: D.-W. Sun (Ed.), Modern Techniques for Food Authentication, second ed., Academic Press, 2018, pp. 219-52 (Chapter 7). Copyright (2018), Elsevier.*

According to the Jablonski diagram the energy of the emission is lower than that of excitation, thus the fluorescence emission is shifted to higher wavelengths compared to the absorption spectrum. The difference between the excitation and emission wavelengths is known as the Stoke's shift. Different molecules have different abilities to convert absorbed photons into fluorescence emission. This efficiency is described by the quantum yield or quantum efficiency (φ) that shows how much of the absorbed light is emitted, and is given by the following equation:

$$\varphi = \frac{number\ of\ emitted\ photon}{number\ of\ absorbed\ photons} \tag{17.11}$$

The higher the value of φ the higher the fluorescence of a compound. A nonfluorescent molecule is one whose quantum efficiency is zero [45, 46]. Another characteristic property of fluorophores is the fluorescence lifetime, τ, which corresponds to the average time that an excited-state electron remains in the excited state before relaxing to the ground state, and is given by the following equation:

$$\tau = \frac{1}{K_r - K_{nr}} \tag{17.12}$$

where K_r and K_{nr} are the rates of the photon emission and the nonradiative decay process, respectively [46].

Among the various processes that can affect the fluorescence intensity of a sample is fluorescence quenching, which refers to any process that leads to a decrease in the fluorescence intensity of a sample, caused by the deactivation of the excited molecules either via intra or intermolecular interactions. Another important parameter affecting the fluorescence intensity is the local environment (solvent, temperature, pH) of the sample. For example, an increase of the solution temperature will enhance the movement and therefore, the collisions among the molecules result in a decrease of the fluorescence intensity. Finally, scattering of the incident light affects the fluorescence signal, especially in turbid solutions where the amount of scattered and reflected light can affect the measurements considerably [45].

A spectrofluorometer contains a light source (xenon or mercury lamp), a monochromator and/or filter(s) for selecting the excitation wavelengths, a sample holder, a monochromator and/or filter(s) for selecting the emission wavelengths, a photodetector that transforms the emitted light to an electrical signal, and a unit for data acquisition and analysis [45].

Fluorescence spectroscopy is a useful technique to characterize fluorescent nanoparticles and quantum dots. Semiconductor nanocrystals show the so-called quantum confinement effect, resulting in enhance light absorption and luminescence, and an emission shift to higher energies as the size of the nanoparticles decreases. As a result, fluorescence spectroscopy allows determining the size of QDs, by measuring the color emitted from nanoparticles of the same building block but different sizes [4].

As the size of the nanoparticles decreases, the bandgap increases and the emission occurs at shorter wavelengths (Fig. 17.13). This shift in the fluorescence wavelength can be used to investigate the bandgap and purity of the nanomaterials [44]. Furthermore, fluorescence spectroscopy can be employed to study the interactions between molecules, such as proteins and QDS, or metallic nanoparticles. For example, the interactions between bovine serum albumin (BSA) and Ag or ZnO nanoparticles have been investigated and showed the formation of protein nanoparticle complexes and the fluorescence quenching of BSA by ZnO [48, 49].
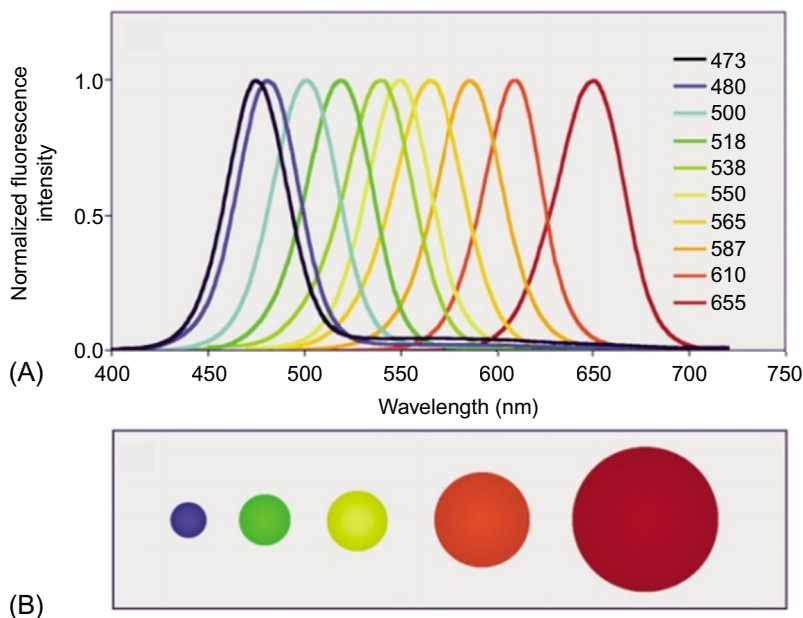
FIG. 17.13 Size-tunable fluorescence spectra of CdSe quantum dots (A) and illustration of the relative particle sizes (B) [47]. *Reproduced with permission from A.M. Smith, S. Nie, Chemical analysis and cellular imaging with quantum dots, Analyst 129 (2004) 672–677. Copyright (2004), Royal Society of Chemistry.*

17.5 Magnetic properties

The magnetic properties of nanoparticles are significantly affected by their size, size distribution, shape, chemical composition, and aggregation state. Two main features that dominate the magnetic properties of nanoparticles are (a) finite-size effects (single-domain or multidomain structures and quantum confinement of the electrons) and (b) surface effects, which result from the symmetry breaking of the crystal structure at the surface of the particle due to oxidation, dangling bonds, presence of surfactants, surface strain, or even different chemical and physical structures present in the internal-core or surface-shell of the nanoparticles [50, 51].

The magnetic properties of the nanoparticles can be investigated by measuring the magnetization (M) as a function of the magnetic field (H) in an M-H hysteresis loop. These measurements are usually carried out by magnetometers such as the superconducting quantum-interference-device magnetometer (SQUID), or the vibrating sample magnetometer (VSM). The characteristic features of these curves are linked to the type of material, the size, and the shape of the magnetic nanoparticles [4, 51, 52].

Measurements are obtained by recording the magnetization of the sample following its saturation in fields up to 5–7 T at different temperatures, between 5 and 300 K, under a DC (direct current) or AC (alternate current) field. Samples in a powder form can be pressed into small pellets, whereas liquid samples are measured as is. Solid samples are placed in a tightly closed sample holder (glass capillary or plastic) while maintaining the temperature below its

FIG. 17.14 A typical magnetization hysteresis loop of a ferromagnetic material [4]. *Reproduced with permission from A. Barhoum, M. Luisa García-Betancourt, Physicochemical characterization of nanomaterials: size, morphology, optical, magnetic, and electrical properties, in: A. Barhoum, A.S.H. Makhlouf (Eds.), Emerging Applications of Nanoparticles and Architecture Nanostructures, Elsevier, 2018, pp. 279–304 (Chapter 10). Copyright (2018), Elsevier.*
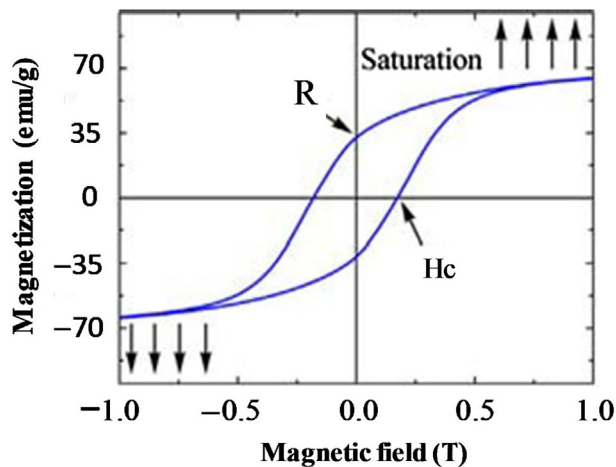
frozen temperature, however, liquids are embedded in a piece of cotton after drying. Magnetic hysteresis loops are acquired at a constant temperature by sweeping an applied magnetic field from zero to a maximum value, H_{max}, and then sweeping to field to $-H_{max}$ and back to zero (Fig. 17.14). In superparamagnetic nanoparticles, the effective magnetic size can be obtained by calculating the magnetic moment of the sample, estimated by fitting the measurements to a Langevin magnetization model, weighted by a log-normal distribution. However, the nanoparticles may not strictly obey Langevin behavior due to their orientation and magnetic interactions. Furthermore, chemical modification of the nanoparticles, such as the use of surface coatings, can also cause changes in their magnetic behavior [51].

Zero-field cooling (ZFC) and field cooling (FC) curves can be used to determine the magnetic irreversibility and blocking temperatures (T_B) of magnetic nanoparticles. To obtain these curves the sample is first cooled to a desired temperature and a magnetic field H_0, is applied, after which magnetization as a function of temperature is measured while warming the sample (zero-field cooled, ZFC). When a higher temperature is reached, the system is cooled with the magnetic field in the "on" state ("field cooling," FC) [51].

AC susceptibility can be also determined by measuring the time-dependent magnetic moment that results after applying an alternating magnetic field to the sample. AC susceptibility characterizes the Neel and Brown relaxation processes, as it can follow the blocking temperatures as a function of the frequency in a large range [52].

Ferromagnetic resonance (FMR) is another powerful spectroscopic technique used to measure the magnetic properties of nanostructured materials. Ferromagnetic resonance (FMR) probes the magnetization of a ferromagnetic material placed in an external magnetic field, which results from the magnetic moments of the dipolar coupled, unpaired electrons. During the resonance process, energy is absorbed from an rf transverse magnetic field h_{rf}, when its frequency matches the precessional frequency (ω). By FMR, important characteristics of the material such as the Curie temperature, total magnetic moment, relaxation mechanism, elementary excitations, and others can be measured. FMR is a very sensitive technique that requires only a few nanograms of the material [52, 53].

Mössbauer spectroscopy is another absorption technique often used to study the magnetic properties of nanomaterials by probing a nucleus with gamma rays made from radioelements. It is mainly used for materials bearing iron, however, it has also been used for gold-containing materials. The technique is based on the Doppler effect in varying the incident energy when the source is set in motion allowing to scan the energy range and investigate slight changes in the resonance line of the probed element, which reflects its environment. In general, three types of nuclear interactions are probed (a) isomer shift (or chemical shift), (b) quadrupolar splitting, and (c) hyperfine splitting (Zeeman splitting). The isomer shift is sensitive to the oxidation state of the element and is correlated with the electron charge density in the s orbital. Quadrupolar splitting shows the influence of surrounding field gradients and nuclear energy levels while magnetic splitting (hyperfine splitting) originates from the interactions between the nucleus and the local magnetic field. Mössbauer spectroscopy can provide the oxidation state of the element, the local symmetry around the atoms at different positions in the structure, and the magnetic order, as reflected by the hyperfine magnetic field. The technique can also provide information about the superparamagnetic behavior of the sample since the collapse of the hyperfine field determines the blocking temperature [52, 54].

Finally, magnetic force microscopy (MFM) is a surface detection technique, a special mode of operation of AFM that employs a magnetic probe to characterize magnetic materials. In MFM, a magnetically coated tip is used to scan the sample surface, and as the tip interacts magnetically with the magnetic domains of the sample an MFM signal is produced (Fig. 17.15A) [55]. In comparison to other magnetometry methods, MFM can map the local stray fields originating from individual nanostructures, thus providing insight into their magnetic behavior. MFM can simultaneously provide information about the topography and the static magnetic configuration of individual magnetic nanostructures. MFM is extensively employed to probe the position of magnetic nanoparticles. For example, magnetic ferritin nanoparticles embedded in a film (Fig. 17.15B) appeared dark compared to the rest of the nonmagnetic material [56]. MFM has been also used to detect biomolecules by labeling them with magnetic nanoparticles [58] and to investigate the cellular uptake of magnetic nanoparticles [57]. In one example, MFM was used to investigate antisense oligonucleotides (ASOs) uptake by human leukemia (HL-60) cells by labeling the oligonucleotide with silica-coated magnetic iron oxide nanoparticles (SMNPs) (Fig. 17.15C–E) [57].

17.6 Composition, chemical structure, and substructure

17.6.1 Nuclear magnetic resonance spectroscopy

Nuclear magnetic resonance (NMR) spectroscopy is a nondestructive/noninvasive technique that takes advantage of the magnetic properties of the nucleus to sense the chemical environment of a nucleus in a molecular structure. NMR can operate both in the liquid and the solid-state, in one-dimensional (1D), two-dimensional (2D), and multidimensional (nD) experiments providing information about the structure, composition, purity, molecular weight, dynamics, and diffusion properties of nanomaterials Furthermore, with the latest developments in NMR spectroscopy, suspension and colloidal nanomaterials can be also investigated [59].
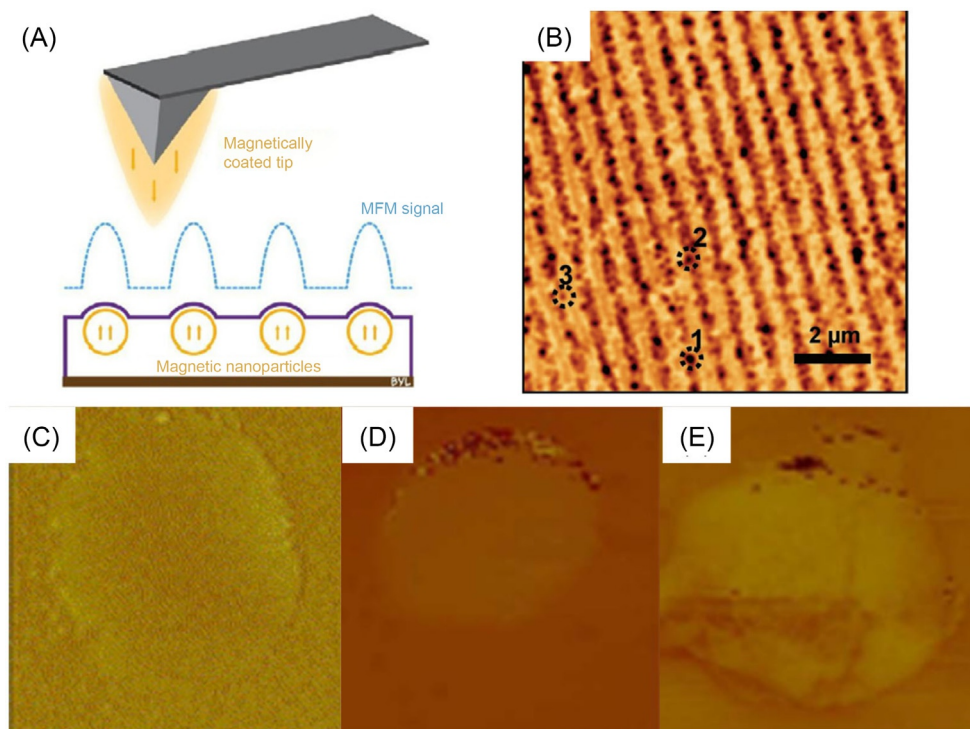
FIG. 17.15   Schematic representation of magnetic force microscopy (A) [55], MFM image of ferritin nanoparticles (the different magnetic contrast is associated with the cluster size, with the larger particles presenting the strongest magnetic contrast and appear darker) (B) [56] and of HL-60 cell (C), cell treated with SMNPs (D) and cell treated with ASOs-coupled SMNPs (E) [57]. *Reproduced with permission from G. Cordova, B. Yasie Lee, Z. Leonenko, Magnetic force microscopy for nanoparticle characterization, NanoWorld J. (2016). Copyright (2016), R.V. Martinez, M. Chiesa, R. Garcia, Nanopatterning of ferritin molecules and the controlled size reduction of their magnetic cores, Small 7 (2011) 2914–2920. Copyright (2011), John Wiley & Sons, H.-b. Shen, D.-h. Long, L.-z. Zhu, X.-y. Li, Y.-m. Dong, N.-q. Jia, et al., Magnetic force microscopy analysis of apoptosis of HL-60 cells induced by complex of antisense oligonucleotides and magnetic nanoparticles, Biophys. Chem. 122 (2006) 1–4. Copyright (2006), Elsevier.*

NMR spectroscopy is based on the interaction of radio-frequency (MHz) electromagnetic radiation with nuclei of atoms immersed in a strong magnetic field. The fundamental idea of NMR spectroscopy is based on the magnetic properties of the nuclei of atoms. Subatomic particles such as electrons, protons, and neutrons can be imagined as spinning about their axes. Due to the circulation of charge, the positively charged spinning nucleus behaves like a tiny bar magnet generating a magnetic dipole along the direction of the spin axis. Nuclei with an odd mass or odd atomic number have *nuclear spin quantum number m* (similar to the spin of electrons). ^{1}H, ^{13}C, ^{15}N, ^{19}F, ^{29}Si are examples of nuclei that have a spin number $I = 1/2$ while nucleus with even atomic mass and atomic number (such as ^{12}C, ^{16}O) have nucleus spin $I = 0$, and are NMR inactive [59–61]. A nucleus with a nucleus spin I, adopts $2I + 1$ orientation, upon the application of a magnetic field. Each orientation corresponds to an energy level that is labeled by a magnetic quantum number m ($m = -I$ to $+I$). For example, a nucleus with nuclear
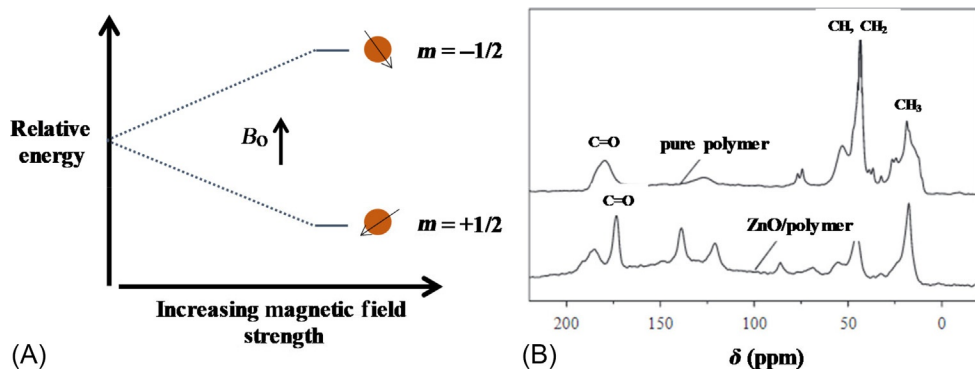
FIG. 17.16 Nuclear Zeeman effect for a nucleus with $I=\frac{1}{2}$ (A) and solid-state ^{13}C NMR spectra of hybrid nanoparticles and the pure polymer (B) [62]. *Reproduced with permission from E. Tang, G. Cheng, X. Ma, Preparation of nano-ZnO/PMMA composite particles via grafting of the copolymer onto the surface of zinc oxide nanoparticles, Powder Technol. 161 (2006) 209–214. Copyright (2006), Elsevier.*

spin 1/2 exhibits two possible orientations one in the same ($m=+1/2$) and another in opposing direction ($m=-1/2$) to the externally applied magnetic field. In the absence of an external magnetic field, these orientations are of equal energy, but upon the application of an external magnetic field, they separate in energy, with the largest positive m value corresponding to the lowest energy (more stable) state. This energy splitting induced by the external static magnetic field is called the "nuclear Zeeman effect (Fig. 17.16A)" [60, 61]. The energy of each spin state, E_i, is directly proportional to m_i and the strength of the magnetic field, B_0, and is given by the following equation [60]:

$$E_i = -m_i \frac{\gamma h B_0}{2\pi} \tag{17.13}$$

where h is the Planck's constant, and γ is the magnetogyric ratio, a constant that is characteristic for each isotope and describes the variation of the spin state energies of a given nucleus with the changes in the external magnetic field. The difference in energy between any two nuclear spin states increases proportionally with the strength of the applied magnetic field. For a nucleus with $I=1/2$, the energy difference of the two nuclear spin states is given by the equation [60]:

$$\Delta E = \frac{\gamma h B_0}{2\pi} \tag{17.14}$$

The rotational axis of the spin nucleus is not aligned exactly parallel or antiparallel to the external magnetic field instead, they wobble about the axis of the applied field at an angle with an angular velocity ω. This periodic wobbling motion is called precession. The frequency of precession is also known as "Larmor frequency" and depends on the gyromagnetic ratio γ of the nucleus and the applied field according to the equation [60, 61]:

$$\omega = \gamma B_0 \tag{17.15}$$

II. Nanotechnology

The energy difference of the spin states is small, thus energy from thermal collisions is sufficient to place many nuclei into the higher energy spin states. The Boltzmann distribution between the spin energy states depends on the temperature, magnetic field strength, and the gyromagnetic radio. The signal intensity of any spectroscopic technique depends largely on the population change between the two energy levels. In NMR, the energy separation of the spin states is relatively small, and in general, the difference of the nuclei populations in the different spin states is very small but can increase with the strength of the magnetic field. Thus, compared to other absorption techniques, NMR spectroscopy is considered as a less sensitive technique [60, 61].

Irradiation of a sample immersed in a magnetic field with radiowaves (MHz) causes the nuclei to absorb energy and thus, change the orientation of nuclear spins from the low-energy spin state to the high-energy spin state. The absorption of energy occurs when the frequency of the radiation matches (resonates) with the frequency of precession. Once the applied field is removed, the nuclei relax back to their lower energy state, releasing the extra energy. This energy is recorded to obtain the characteristic fingerprint spectra of a given molecule [60, 61].

The two common methods in NMR spectroscopy are the Fourier transform NMR spectroscopy and the continuous-wave NMR spectroscopy. Fourier transform NMR spectrometers use the pulse of radiofrequency (RF) for the measurements. The basic components of an RF NMR spectrometer are the RF source and the magnetic field. The sample is placed in a probe, which is positioned between the poles of a magnet. If the frequency of the RF irradiation is held constant and the strength of the applied magnetic field is varied, each nucleus comes into resonance at a slightly different field strength. A sensitive detector monitors the absorption of RF energy, and its electronic signal is then amplified and displayed as a peak [61].

NMR spectroscopy is mainly used to characterize samples in the liquid state, however, recent progress, such as magic angle spinning (MAS), high-resolution magic angle spinning (HR-MAS), cross-polarization (CP), and cross-polarization magic angle spinning (CP-MAS) have opened new horizons for solid-state NMR experiments. Furthermore, some of the most popular NMR methods, that is, correlation spectroscopy (COSY), heteronuclear single quantum correlation spectroscopy (HSQC), heteronuclear multiple bond quantum correlation spectroscopy (HMBC), total quantum coherence spectroscopy (TOCSY), exchange spectroscopy (EXSY), and diffusion-ordered spectroscopy (DOSY), in combination with other techniques such as magnetic resonance imaging (MRI) and magnetic resonance scanning (MRS) have been developed for both solution and solid-state samples [59].

NMR can be employed to determine the composition of block copolymer-based micellar nanoparticles and to characterize the structure and physical properties of dendritic nanoparticles, carbon nanotubes, nanocrystalline hydroxyapatite, zinc oxide, and polymeric nanoparticles in inorganic–organic composites. Solid-state ^{13}C NMR has been employed to characterize the interactions between ZnO and a poly(methyl methacrylate)-poly(acrylic acid) copolymer in composite nanohybrids, where the change of the chemical shift of the C=O bond of the copolymer from 180.7 to 173.4 ppm, suggest a strong interaction between ZnO and the carboxyl groups of the copolymer chains [59, 62] (Fig. 17.16B). However, CP-MAS-DNP NMR of ^{113}Cd, ^{77}Se, and ^{133}Cs have been used to determine the chemical composition of quantum dots [59, 63]. Moreover, 2D NMR ^{1}H-^{1}H COSY, ^{13}C-^{1}H HSQC under different MAS rates, and ^{1}H DOSY can characterize different types of organic molecules bound to nanoparticles [59]. DOSY is used to determine

the size of polymers and nanoparticles and the critical micelle concentration of amphiphilic di-block copolymers and to estimate the amount of encapsulated small molecules within nanoparticles [61].

17.6.2 X-ray diffraction

X-ray diffraction (XRD) is used to study the crystalline structure of materials since the X-ray wavelengths (between 0.2 and 10 nm) are comparable to the interatomic spacing of crystalline solids. The technique measures the average spacing between layers or rows of atoms. XRD allows us to determine the orientation of a single crystal or grain and to measure the size and shape of small crystalline regions [7].

In XRD, a collimated beam of X-rays is scattered by the periodic lattice of the sample, as a result of the interactions of the photons with the electrons of the material using an elastic and coherent scattering process [64].

Each crystalline material has a discreet atomic structure, which upon irradiation with X-rays causes a constructive and destructive interference of the scattered X-ray beam, generating a unique diffraction pattern that presents several sharp spots, known as Bragg diffraction peaks. Typical diffraction patterns of crystalline and amorphous material are presented in Fig. 17.17A. The XRD of the crystalline sample reveals the presence of well-defined peaks at specific scattering angles, while the amorphous sample shows an intensity maximum that extents over several degrees (2θ) [64]. The diffraction of X-rays by a crystal is described by the Bragg law that relates the wavelength of the X-rays to the interatomic spacing, and is given by the following equation:

$$2d\sin\theta = n\lambda \tag{17.16}$$

where d is the perpendicular distance between pairs of adjacent planes, θ is the angle of incidence or Bragg angle, λ is the wavelength of the beam, and n denotes an integer number, known as the order of the reflection and is the path difference, in terms of wavelength, between waves scattered by adjacent planes of atoms [7].
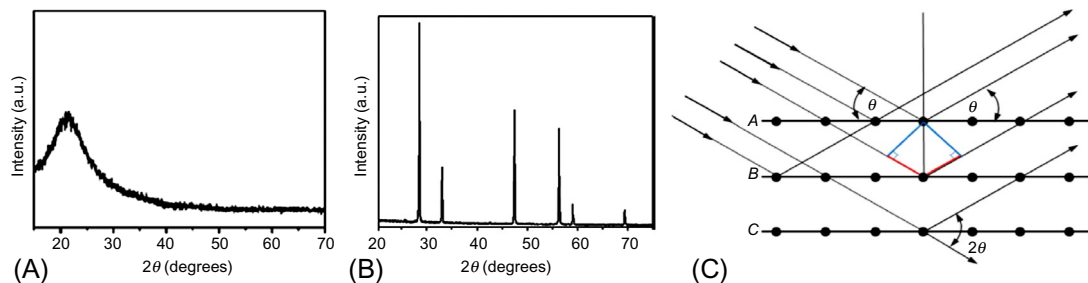

FIG. 17.17   XRD patterns of an amorphous (A) and a crystalline (B) material and (C) schematic representation of reflections from adjacent planes within the crystal [64]. *Reproduced with permission from D.G. Lamas, M. de Oliveira Neto, G. Kellermann, A.F. Craievich, X-ray diffraction and scattering by nanomaterials, in: A.L. Da Róz, M. Ferreira, F. de Lima Leite, O.N. Oliveira (Eds.), Nanocharacterization Techniques, William Andrew Publishing, 2017, pp. 111–182 (Chapter 5). Copyright (2017), William Andrew Publishing.*

X-rays generate when electrically charged particles with sufficient energy are accelerated toward an anode. For the generation of an X-ray beam, a vacuum tube is needed where an electron beam, produced by a heated filament, is collimated and accelerated by an electric potential of 20–45 kV. This electron beam is directed toward the metallic anode. The anode is kept in a high vacuum chamber to avoid collisions between air particles and either the incident electrons or the emitted X-ray photons. The absorption of X-ray which passes through the material depends on the atomic weight of the elements present in the material. X-rays are detected by the detector, and the signals are processed with a microprocessor or electronically. A spectrograph is obtained by altering the angle between the source, sample, and detector [2, 7].

XRD can provide additional information regarding the crystallite size. The average crystallite size can be calculated by the peak broadening of the diffraction peaks using the Scherrer equation:

$$t = K\lambda/\beta cos\theta \tag{17.17}$$

where t is the crystallite size, λ is the wavelength of the incident X-ray beam, β is the full width at half of the maximum intensity of the reflection peak, and K is the Scherrer constant [7].

XRD is in general useful for nanoscale crystallites with diameters below 100–200 nm since peak broadening is negligible for bigger particles. On the other hand, for very small particles with a diameter below 2–3 nm the peak broadening becomes so severe that the peak width cannot be measured accurately or even sometimes detected. Furthermore, the Scherrer constant K in Eq. (17.17) represents the shape of the particles and obtains a value of 0.9 for spherical particles, while it varies for anisotropic particles.

In general, XRD is less informative for anisotropic particles and particles with a nonuniform size distribution, thus in such cases, it should be interpreted with additional analyses such as TEM. Furthermore, it is not possible to characterize individual particles by XRD and the equation discussed earlier determines the average particle size for material and not the actual particle size [7]. Moreover, the Scherrer equation does not consider internal particle strain and defects, which can also lead to peak broadening, and therefore, the particle size measured by XRD should not be considered as an absolute measure of the crystallite size but rather as the lower limit [7, 33].

Finally, XRD patterns can be used to obtain the elemental ratio of a mixture, the degree of crystallinity, and the deviation of a particular component from its ideal composition and/or structure [2]. Recently, in-situ XRD has been developed as a characterization technique in mechanistic and kinetic studies to follow the reaction progress in real-time [4].

17.6.3 X-ray photoelectron spectroscopy

X-ray photoelectron spectroscopy (XPS), also known as X-ray photoemission spectroscopy, is a quantitative spectroscopic surface analysis technique used to determine the elemental composition, chemical, and electronic state of the atoms within a material, with an atomic sensitivity of 0.1%–1% [4, 65]. XPS gives elemental and chemical information for all the elements present on the surface of a sample except for H and He. XPS can be also employed to estimate the oxidation states of the elements present in a material with an average depth analysis of

about 1–10 nm [33]. Therefore, XPS is a potent nondestructive surface-sensitive technique that allows to investigate the surface chemistry of nanoparticles, nanostructured materials, surfaces, coatings, and thin films [4].

XPS utilizes X-rays to emit electrons from the core orbitals of the elements. An X-ray source, often AlK_α or MgK_α, interacts with the sample surface resulting in the emission of a core level electron with fixed binding energy. The kinetic energy and the number of photoelectrons that are emitted from the sample surface are then measured using an electron energy analyzer. From the kinetic energy, the binding energy of the electrons can be determined using the following equation

$$E_{binding} = E_{photon} - (E_{kinetic} + \Phi) \tag{17.18}$$

where $E_{binding}$ is the energy of the emitted electrons, E_{photon} is the X-ray photon energy, $E_{kinetic}$ is the kinetic energy of the emitted electrons measured by the electron energy analyzer, and Φ is the work function of the electron energy analyzer [4, 65].

The energy spectrum of the photoelectrons shows the electronic structures of the atoms since each element produces a set of XPS peaks at characteristic binding energy values. In general, the binding energy increases by increasing the atomic number of the elements, being roughly proportional to the square of the atomic number [65]. Furthermore, the binding energy is affected by the chemical environment, causing small shifts in the position of the XPS peaks in the spectrum, known as chemical-shifts. For example, the peak position of the Si 2p electrons for a Si—Si bonding state is observed around 99 eV, while for the SiO_2 bonding state the peak is shifted to 103 eV. Therefore, from the binding energy spectrum, the element identification and the oxidation state of the elements can be determined (Fig. 17.18) [66], while quantitative elemental information can be obtained by measuring the peak heights or the integrated area under a given elemental peak [33, 65]. XPS usually operates under high vacuum or ultra-high vacuum conditions, however, recently ambient-pressure XPS was developed in which the samples were measured at intermediate pressures of a few tens of millibars [4]. XPS measures the photoelectrons of the atoms that are within a few nanometers from the sample surface and is a useful tool for the characterization of surfaces providing information that cannot be obtained by techniques with a deeper analysis volume, such as SEM-EDX [4], although, the XPS analysis of a nonconductive material requires special care because such materials generally create unwanted shifts in the energy spectrum [65].

17.7 Mechanical properties

The measurement of the mechanical properties of nanomaterials is challenging since the traditional techniques used for the mechanical characterization of materials at the macroscale are not suitable at the micro or nanoscale. Novel techniques have been developed for the mechanical characterization of nanomaterials [67]. Among them a new attractive method to determine the mechanical properties of nanomaterials is nanoindentation. Nanoindentation, also known as instrumented indentation, is a depth-sensing technique that can provide valuable information from a small sample volume by the indenter load and displacement. In this method, a hard tip is pressed into the sample surface, with a known load, and is then removed (Fig. 17.19A).

FIG. 17.18 Typical XPS spectra of Fe^{2+} for magnetite *(solid line)*, maghemite *(dashed line)*, and hematite *(dashed-dot line)* [66]. *Reproduced with permission from T. Radu, C. Iacovita, D. Benea, R. Turcu, X-ray photoelectron spectroscopic characterization of iron oxide nanoparticles, Appl. Surf. Sci. 405 (2017) 337–343. Copyright (2017), Elsevier.*
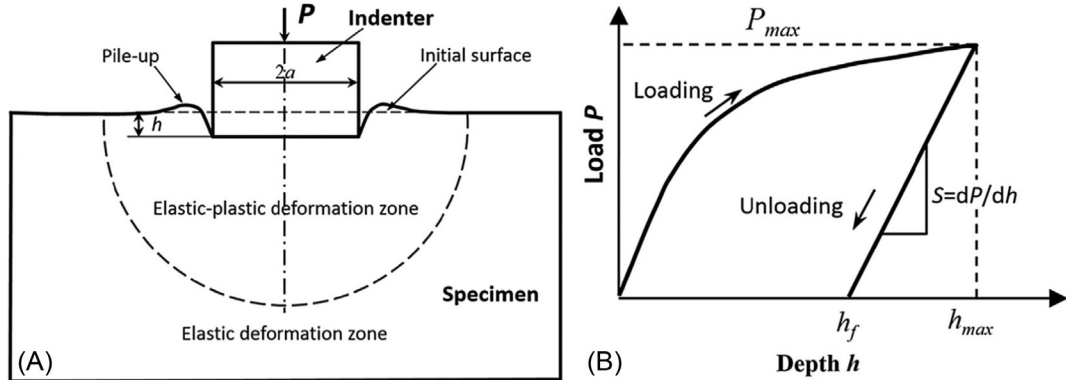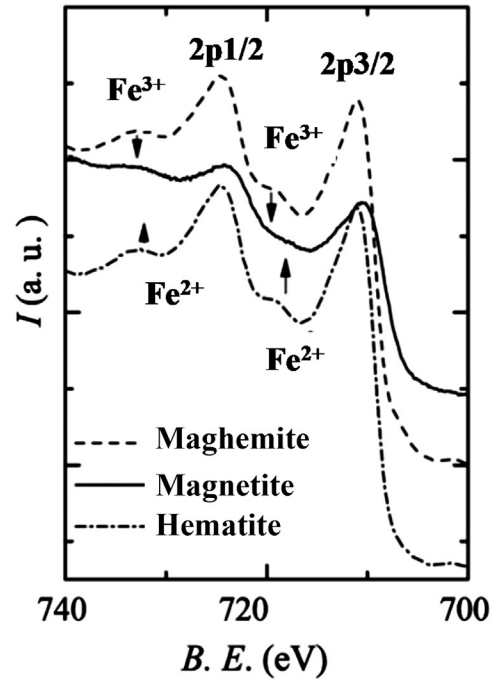

FIG. 17.19 Schematic representation of a nanoindentation experiment using a Berkovich pyramid-shaped tip indenter (A) and load vs depth profile (B) [68]. *Reproduced with permission from Z. Hu, Characterization of materials, nanomaterials, and thin films by nanoindentation, in: S. Thomas, R. Thomas, A.K. Zachariah, R.K. Mishra (Eds.), Microscopy Methods in Nanomaterials Characterization, Elsevier, 2017, pp. 165–239 (Chapter 6). Copyright (2017), Elsevier.*

The penetration of the tip is measured as a function of load and time. Special devices, nanoindenters, operate at loads that range from several tens of μN to N, and penetrations from tens of nanometer to several tenths of a millimeter. The load area can be as small as a fraction of a millimeter square. Most nanoindentation measurements use a simple load-unload cycle as shown in Fig. 17.19B [69].

The experimental load-penetration depth curves contain useful information allowing us to determine the hardness, residual strain, Young's modulus, and toughness of the material. Important parameters during the nanoindentation measurements are the approach speed, the contact load, the maximum load, and the load rate. The Young's modulus of the samples is calculated from the following equation [68]:

$$\frac{1}{E_r} = \frac{1 - v^2}{E} + \frac{1 - v_i^2}{E_i} \tag{17.19}$$

where E and E_i is Young's modulus of the sample and the diamond, respectively, and v_i and v are the Poisson's ratio of the diamond and the sample, respectively. E_r is the reduced Young's modulus and is obtained from the following equation:

$$E_r = \frac{S}{2\beta} \sqrt{\frac{\pi}{A_p(Ah_c)}} \tag{17.20}$$

where S is the stiffness of the sample, β is a constant that depends on the geometry of the indenter of the order of unity (β is equal to 1 for circular contact and 1.05 for the Berkovich indenter), $A_p(Ah_c)$ is the projected area of the indentation at the contact depth h_c. The stiffness is obtained from the slope dP/dh of the upper one-third to one-half of the unloading data, while the contact depth, h_c, is determined from the following equation:

$$h_c = h_{max} - \frac{3P_{max}}{4S} \tag{17.21}$$

where P_{max} and h_{max} are the maximum applied load and contact depth, respectively [68].

Hardness (H) is defined as the ratio of P_{max}/A_p. The elastic displacement during uploading can be determined from the equation:

$$P = 2aE_rh \tag{17.22}$$

where a is the contact radius, which is fixed for the given tip, and for the case of a cylindrical flat tip is equal to the radius of the indenter [68].

The P-h curves can also provide information about the energies involved in the process such as the total work of indentation, W_{tot}, the elastic work, W_{el}, released during unloading, and the plastic work, W_{pl}, which is the energy dissipated during indentation. These energy components give information about the plastic properties of the nanomaterials [69].

Nanoindentation is considered the most powerful technique for measuring mechanical properties at the nanoscale, and modern nanoindentation instruments are very accurate. However, results obtained from similar experiments on similar materials in different laboratories can be different from one another for several reasons: (a) the deformation processes that occur during indentation are complex, (b) measurement and data analysis methods are not standardized, and (c) several experimental parameters can significantly affect the results [70]. Nanoindentation is usually employed to determine the mechanical properties of thin films and coatings, nanoparticles, and fibers as well as patterned structures. In Fig. 17.20 the load-displacement curves of thin poly(acrylonitrile-*co*-methyl methacrylate) films with different polyacrylonitrile (PAN) content are presented. From these curves, one can reveal that for the same penetration depth, the increase in polyacrylonitrile content leads to an increase of the maximum load, indicating a higher stiffness and higher resistance to plastic deformation [71].
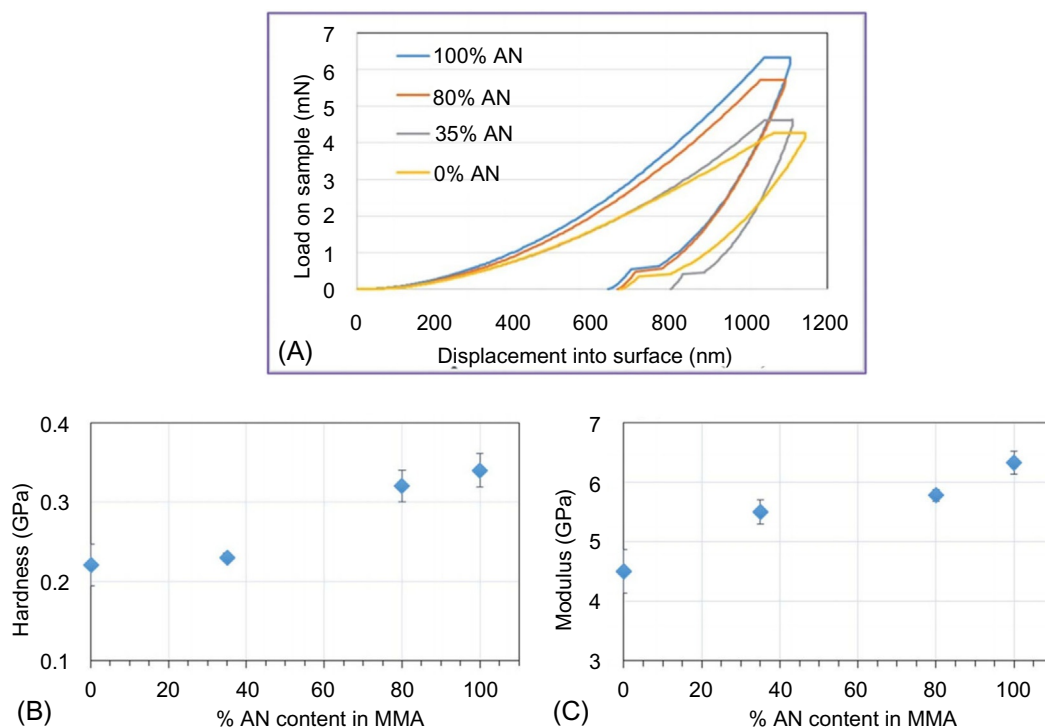
FIG. 17.20 Load-displacement curves of poly(acrylonitrile-*co*-methyl methacrylate) films with different PAN content (A) hardness (B), and modulus (C) as a function of PAN content [71]. *Reproduced with permission from N. Gupta, R. Rai, A. Sikder, S. Nandi, A. Tanwar, R. Khatokar, et al., Design and development of a poly(acrylonitrile-co-methyl methacrylate) copolymer to improve the viscoelastic and surface properties critical to scratch resistance, RSC Adv. 6 (2016) 37933–37937. Copyright (2016), Royal Society of Chemistry.*

References

[1] P.-C. Lin, S. Lin, P.C. Wang, R. Sridhar, Techniques for physicochemical characterization of nanomaterials, Biotechnol. Adv. 32 (2014) 711–726.

[2] D. Titus, E. James Jebaseelan Samuel, S.M. Roopan, Nanoparticle characterization techniques, in: A.K. Shukla, S. Iravani (Eds.), Green Synthesis, Characterization and Applications of Nanoparticles, Elsevier, 2019, pp. 303–319 (Chapter 12).

[3] R.A. Shanks, Characterization of nanostructured materials, in: S. Thomas, R. Shanks, S. Chandrasekharakurup (Eds.), Nanostructured Polymer Blends, William Andrew Publishing, Oxford, 2014, pp. 15–31 (Chapter 2).

[4] A. Barhoum, M. Luisa García-Betancourt, Physicochemical characterization of nanomaterials: size, morphology, optical, magnetic, and electrical properties, in: A. Barhoum, A.S.H. Makhlouf (Eds.), Emerging Applications of Nanoparticles and Architecture Nanostructures, Elsevier, 2018, pp. 279–304 (Chapter 10).

[5] R. Pecora, Dynamic light scattering measurement of nanometer particles in liquids, J. Nanopart. Res. 2 (2000) 123–131.

[6] A.P. Ramos, Dynamic light scattering applied to nanoparticle characterization, in: A.L. Da Róz, M. Ferreira, L.F. de Lima, O.N. Oliveira (Eds.), Nanocharacterization Techniques, William Andrew Publishing, 2017, pp. 99–110 (Chapter 4).

[7] P.H. Salame, V.B. Pawade, B.A. Bhanvase, Characterization tools and techniques for nanomaterials, in: B.A Bhanvase, V.B. Pawade, S.J. Dhoble, S.H. Sonawane, M. Ashokkumar (Eds.), Nanomaterials for Green Energy, Elsevier, 2018, pp. 83–111 (Chapter 3).

[8] D.K. Carpenter, Dynamic Light Scattering with Applications to Chemistry, Biology, and Physics (Berne, Bruce J.; Pecora, Robert), J. Chem. Educ. 54 (1977) A430.

[9] J.B. Berne, R. Pecora, Dynamic Light Scattering: With Applications to Chemistry, Biology, and Physics, John Wiley & Sons Inc, 2000.

[10] J.R.S. Martin, I. Bihannic, C. Santos, J.P.S. Farinha, B. Demé, F.A.M. Leermakers, et al., Structure of multi-responsive brush-decorated nanoparticles: a combined electrokinetic, DLS, and SANS study, Langmuir 31 (2015) 4779–4790.

[11] X. Ye, C. Zhu, P. Ercius, S.N. Raja, B. He, M.R. Jones, et al., Structural diversity in binary superlattices self-assembled from polymer-grafted nanocrystals, Nat. Commun. 6 (2015) 10052.

[12] E.J. Guidelli, A.P. Ramos, M.E.D. Zaniquelli, P. Nicolucci, O. Baffa, Synthesis and characterization of silver/alanine nanocomposites for radiation detection in medical applications: the influence of particle size on the detection properties, Nanoscale 4 (2012) 2884–2893.

[13] M. Yokoyama, A. Satoh, Y. Sakurai, T. Okano, Y. Matsumura, T. Kakizoe, et al., Incorporation of water-insoluble anticancer drug into polymeric micelles and control of their particle size, J. Control. Release 55 (1998) 219–229.

[14] M. Zaru, S. Mourtas, P. Klepetsanis, A.M. Fadda, S.G. Antimisiaris, Liposomes for drug delivery to the lungs by nebulization, Eur. J. Pharm. Biopharm. 67 (2007) 655–666.

[15] S.K. Brar, M. Verma, Measurement of nanoparticles by light-scattering techniques, TrAC Trends Anal. Chem. 30 (2011) 4–17.

[16] C. Jose Chirayil, J. Abraham, R. Kumar Mishra, S.C. George, S. Thomas, Instrumental techniques for the characterization of nanoparticles, in: S. Thomas, R. Thomas, A.K. Zachariah, R.K. Mishra (Eds.), Thermal and Rheological Measurement Techniques for Nanomaterials Characterization, Elsevier, 2017, pp. 1–36 (Chapter 1).

[17] Pereira-da-Silva M de Assumpção, F.A. Ferri, Scanning electron microscopy, in: A.L. Da Róz, M. Ferreira, L.F. de Lima, O.N. Oliveira (Eds.), Nanocharacterization Techniques: William Andrew Publishing, 2017, pp. 1–35 (Chapter 1).

[18] A. Mayeen, L.K. Shaji, A.K. Nair, N. Kalarikkal, Morphological characterization of nanomaterials, in: S. Mohan Bhagyaraj, O.S. Oluwafemi, N. Kalarikkal, S. Thomas (Eds.), Characterization of Nanomaterials: Woodhead Publishing, 2018, pp. 335–364 (Chapter 12).

[19] Z.L. Wang, J.L. Lee, Electron microscopy techniques for imaging and analysis of nanoparticles, in: R. Kohli, K. L. Mittal (Eds.), Developments in Surface Contamination and Cleaning, second ed., William Andrew Publishing, Oxford, 2008, pp. 395–443 (Chapter 9).

[20] C. Dazon, O. Witschger, S. Bau, V. Fierro, P.L. Llewellyn, Nanomaterial identification of powders: comparing volume specific surface area, X-ray diffraction and scanning electron microscopy methods, Environ. Sci. Nano 6 (2019) 152–162.

[21] F. Li, F. Gong, Y. Xiao, A. Zhang, J. Zhao, S. Fang, et al., ZnO twin-spheres exposed in ±(001) facets: stepwise self-assembly growth and anisotropic blue emission, ACS Nano 7 (2013) 10482–10491.

[22] H. Liu, Z. Huang, J. Huang, S. Xu, M. Fang, Y.-g. Liu, et al., Morphology controlling method for amorphous silica nanoparticles and jellyfish-like nanowires and their luminescence properties, Sci. Rep. 6 (2016) 22459.

[23] M.A.C. Potenza, Ž. Krpetić, T. Sanvito, Q. Cai, M. Monopoli, J.M. de Araújo, et al., Detecting the shape of anisotropic gold nanoparticles in dispersion with single particle extinction and scattering, Nanoscale 9 (2017) 2778–2784.

[24] M. Mohl, D. Dobo, A. Kukovecz, Z. Konya, K. Kordas, J. Wei, et al., Formation of CuPd and CuPt bimetallic nanotubes by galvanic replacement reaction, J. Phys. Chem. C 115 (2011) 9403–9409.

[25] L. Zhang, A. Eisenberg, Formation of crew-cut aggregates of various morphologies from amphiphilic block copolymers in solution, Polym. Adv. Technol. 9 (1998) 677–699.

[26] A.E. Garcia-Bennett, O. Terasaki, S. Che, T. Tatsumi, Structural investigations of AMS-n mesoporous materials by transmission electron microscopy, Chem. Mater. 16 (2004) 813–821.

[27] F. Hofer, P. Warbichler, H. Kronberger, J. Zweck, Mapping the chemistry in nanostructured materials by energy-filtering transmission electron microscopy (EFTEM), Spectrochim. Acta A Mol. Biomol. Spectrosc. 57 (2001) 2061–2069.

[28] R.T. Dombrowski, Microscopy techniques for analyzing the phase nature and morphology of biomaterials, in: M. Jaffe, W. Hammond, P. Tolias, T. Arinzeh (Eds.), Characterization of Biomaterials, Woodhead Publishing, 2013, pp. 1–33 (Chapter 1).

[29] S.Y. Yu-Su, S.S. Sheiko, H.-i. Lee, W. Jakubowski, A. Nese, K. Matyjaszewski, et al., Crystallization of molecular brushes with block copolymer side chains, Macromolecules 42 (2009) 9008–9017.

II. Nanotechnology

[30] M. Baalousha, J.R. Lead, Rationalizing nanomaterial sizes measured by atomic force microscopy, flow field-flow fractionation, and dynamic light scattering: sample preparation, polydispersity, and particle structure, Environ. Sci. Technol. 46 (2012) 6134–6142.

[31] D. Kawaguchi, T. Nishu, A. Takano, Y. Matsushita, Direct observation of an isolated cyclic sodium poly(styrenesulfonate) molecule by atomic force microscopy, Polym. J. 39 (2007) 271–275.

[32] S. Mourdikoudis, R.M. Pallares, N.T.K. Thanh, Characterization techniques for nanoparticles: comparison and complementarity upon studying nanoparticle properties, Nanoscale 10 (2018) 12871–12934.

[33] R.D. Holbrook, A.A. Galyean, J.M. Gorham, A. Herzing, J. Pettibone, Overview of nanomaterial characterization and metrology, in: M. Baalousha, J.R. Lead (Eds.), Frontiers of Nanoscience, Elsevier, 2015, pp. 47–87 (Chapter 2).

[34] K. Pate, P. Safier, Chemical metrology methods for CMP quality, in: S. Babu (Ed.), Advances in Chemical Mechanical Planarization (CMP), Woodhead Publishing, 2016, pp. 299–325 (Chapter 12).

[35] A. Kumar, C.K. Dixit, Methods for characterization of nanoparticles, in: S. Nimesh, R. Chandra, N. Gupta (Eds.), Advances in Nanomedicine for the Delivery of Therapeutic Nucleic Acids, Woodhead Publishing, 2017, pp. 43–58 (Chapter 3).

[36] M.F. Bédard, S. Sadasivan, G.B. Sukhorukov, A. Skirtach, Assembling polyelectrolytes and porphyrins into hollow capsules with laser-responsive oxidative properties, J. Mater. Chem. 19 (2009) 2226–2233.

[37] C. Yang, J. Xiao, W. Xiao, W. Lin, J. Chen, Q. Chen, et al., Fabrication of PDEAEMA-based pH-responsive mixed micelles for application in controlled doxorubicin release, RSC Adv. 7 (2017) 27564–27573.

[38] R. Xu, Progress in nanoparticles characterization: sizing and zeta potential measurement, Particuology 6 (2008) 112–115.

[39] M.S. Jeong, G. Namkoong, C.C. Byeon, J.S. Kim, H.S. Lee, Optical characterization of nanomaterials, J. Nanomater. 2014 (2014) 2.

[40] G. George, R. Wilson, J. Joy, Ultraviolet spectroscopy: a facile approach for the characterization of nanomaterials, in: S. Thomas, R. Thomas, A.K. Zachariah, R.K. Mishra (Eds.), Spectroscopic Methods for Nanomaterials Characterization, Elsevier, 2017, pp. 55–72 (Chapter 3).

[41] S. Linic, P. Christopher, D.B. Ingram, Plasmonic-metal nanostructures for efficient conversion of solar to chemical energy, Nat. Mater. 10 (2011) 911.

[42] P. Alessio, P.H.B. Aoki, L.N. Furini, A.E. Aliaga, C.J. Leopoldo Constantino, Spectroscopic techniques for characterization of nanomaterials, in: A.L. Da Róz, M. Ferreira, L.F. de Lima, O.N. Oliveira (Eds.), Nanocharacterization Techniques, William Andrew Publishing, 2017, pp. 65–98 (Chapter 3).

[43] A.K. Nair, A. Mayeen, L.K. Shaji, M.S. Kala, S. Thomas, N. Kalarikkal, Optical characterization of nanomaterials, in: S. Mohan Bhagyaraj, O.S. Oluwafemi, N. Kalarikkal, S. Thomas (Eds.), Characterization of Nanomaterials, Woodhead Publishing, 2018, pp. 269–299 (Chapter 10).

[44] R.K. Goyal, Characterization of nanomaterials, in: Nanomaterials and Nanocomposites Synthesis, Properties, Characterization Techniques, and Application, Taylor and Francis Group, 2017 (Chapter 12).

[45] R. Karoui, Spectroscopic technique: fluorescence and ultraviolet-visible (UV-Vis) spectroscopies, in: D.-W. Sun (Ed.), Modern Techniques for Food Authentication, second ed., Academic Press, 2018, pp. 219–252 (Chapter 7).

[46] A. Boreham, R. Brodwolf, K. Walker, R. Haag, U. Alexiev, Time-resolved fluorescence spectroscopy and fluorescence lifetime imaging microscopy for characterization of dendritic polymer nanoparticles and applications in nanomedicine, Molecules 22 (2016) 17.

[47] A.M. Smith, S. Nie, Chemical analysis and cellular imaging with quantum dots, Analyst 129 (2004) 672–677.

[48] A. Bhogale, N. Patel, P. Sarpotdar, J. Mariam, P.M. Dongre, A. Miotello, et al., Systematic investigation on the interaction of bovine serum albumin with ZnO nanoparticles using fluorescence spectroscopy, Colloids Surf. B: Biointerfaces 102 (2013) 257–264.

[49] J. Mariam, P.M. Dongre, D.C. Kothari, Study of interaction of silver nanoparticles with bovine serum albumin using fluorescence spectroscopy, J. Fluoresc. 21 (2011) 2193.

[50] B. Issa, I.M. Obaidat, B.A. Albiss, Y. Haik, Magnetic nanoparticles: surface effects and properties related to biomedicine applications, Int. J. Mol. Sci. 14 (2013) 21266–21305.

[51] F. Herranz, M.P. Morales, I. Rodríguez, J. Ruiz-Cabello, Iron oxide nanoparticle-based MRI contrast agents: characterization and in vivo use, in: C.S.S.R. Kumar (Ed.), Magnetic Characterization Techniques for Nanomaterials, Springer Berlin Heidelberg, Berlin, Heidelberg, 2017, pp. 85–120.

[52] J. Alonso, J.M. Barandiarán, L. Fernández Barquín, A. García-Arribas, Magnetic nanoparticles, synthesis, properties, and applications, in: A.A. El-Gendy, J.M. Barandiarán, R.L. Hadimani (Eds.), Magnetic Nanostructured Materials, Elsevier, 2018, pp. 1–40 (Chapter 1).

[53] S.P. Manish Sharma, M. Sharma, FMR measurements of magnetic nanostructures, in: Ferromagnetic Resonance, IntechOpen, 2013 (Chapter 4).

[54] B. Donnio, J.L. Gallani, M.V. Rastei, Characterization of magnetism in gold nanoparticles, in: C.S.S.R. Kumar (Ed.), Magnetic Characterization Techniques for Nanomaterials, Springer Berlin Heidelberg, Berlin, Heidelberg, 2017, pp. 191–207.

[55] G. Cordova, B. Yasie Lee, Z. Leonenko, Magnetic Force Microscopy for Nanoparticle Characterization, arXiv e-prints (2017).

[56] R.V. Martinez, M. Chiesa, R. Garcia, Nanopatterning of ferritin molecules and the controlled size reduction of their magnetic cores, Small 7 (2011) 2914–2920.

[57] H.-b. Shen, D.-h. Long, L.-z. Zhu, X.-y. Li, Y.-m. Dong, N.-q. Jia, et al., Magnetic force microscopy analysis of apoptosis of HL-60 cells induced by complex of antisense oligonucleotides and magnetic nanoparticles, Biophys. Chem. 122 (2006) 1–4.

[58] D. Passeri, C. Dong, M. Reggente, L. Angeloni, M. Barteri, F.A. Scaramuzzo, et al., Magnetic force microscopy, Biomatter 4 (2014) e29507.

[59] N. Agarwal, M.S. Nair, A. Mazumder, K.M. Poluri, Characterization of nanomaterials using nuclear magnetic resonance spectroscopy, in: S. Mohan Bhagyaraj, O.S. Oluwafemi, N. Kalarikkal, S. Thomas (Eds.), Characterization of Nanomaterials, Woodhead Publishing, 2018, pp. 61–102 (Chapter 3).

[60] R.S. Macomber, A Complete Introduction to Modern NMR Spectroscopy, John Wiley & Sons Inc, 1998.

[61] R.K. Mishra, J. Cherusseri, A. Bishnoi, S. Thomas, Nuclear magnetic resonance spectroscopy, in: S. Thomas, R. Thomas, A.K. Zachariah, R.K. Mishra (Eds.), Spectroscopic Methods for Nanomaterials Characterization, Elsevier, 2017, pp. 369–415 (Chapter 13).

[62] E. Tang, G. Cheng, X. Ma, Preparation of nano-ZnO/PMMA composite particles via grafting of the copolymer onto the surface of zinc oxide nanoparticles, Powder Technol. 161 (2006) 209–214.

[63] L. Piveteau, T.-C. Ong, A.J. Rossini, L. Emsley, C. Copéret, M.V. Kovalenko, Structure of colloidal quantum dots from dynamic nuclear polarization surface enhanced NMR spectroscopy, J. Am. Chem. Soc. 137 (2015) 13964–13971.

[64] D.G. Lamas, N.M. de Oliveira, G. Kellermann, A.F. Craievich, X-ray diffraction and scattering by nanomaterials, in: A.L. Da Róz, M. Ferreira, L.F. de Lima, O.N. Oliveira (Eds.), Nanocharacterization Techniques, William Andrew Publishing, 2017, pp. 111–182 (Chapter 5).

[65] T.A. Satoshi Ohara, T. Ida, M. Yashima, T. Mikayama, H. Abe, Y. Setsuhara, K. Nogi, M. Miyahara, K. Kaneko, A. Ohtomo, Characterization methods for nanostructure of materials, in: M. Naito, T. Yokoyama, K. Hosokawa, K. Nogi (Eds.), Nanoparticle Technology Handbook, third ed., Elsevier, 2018, pp. 255–300 (Chapter 5).

[66] T. Radu, C. Iacovita, D. Benea, R. Turcu, X-ray photoelectron spectroscopic characterization of iron oxide nanoparticles, Appl. Surf. Sci. 405 (2017) 337–343.

[67] M.F. Pantano, H.D. Espinosa, L. Pagnotta, Mechanical characterization of materials at small length scales, J. Mech. Sci. Technol. 26 (2012) 545–561.

[68] Z. Hu, Characterization of materials, nanomaterials, and thin films by nanoindentation, in: S. Thomas, R. Thomas, A.K. Zachariah, R.K. Mishra (Eds.), Microscopy Methods in Nanomaterials Characterization, Elsevier, 2017, pp. 165–239 (Chapter 6).

[69] J. Menčík, Nanoindentation techniques for the determination of mechanical properties of materials in dentistry, in: K. Subramani, W. Ahmed (Eds.), Emerging Nanotechnologies in Dentistry, second ed., William Andrew Publishing, 2018, pp. 307–326 (Chapter 15).

[70] S.P. Baker, Nanoindentation techniques, in: K.H.J. Buschow, R.W. Cahn, M.C. Flemings, B. Ilschner, E.J. Kramer, S. Mahajan et al., Encyclopedia of Materials: Science and Technology, Elsevier, Oxford, 2001, pp. 5908–5915.

[71] N. Gupta, R. Rai, A. Sikder, S. Nandi, A. Tanwar, R. Khatokar, et al., Design and development of a poly(acrylonitrile-co-methyl methacrylate) copolymer to improve the viscoelastic and surface properties critical to scratch resistance, RSC Adv. 6 (2016) 37933–37937.